



Characterization of Earth-Moon L2 halo analogs in an ephemeris model using the elliptic restricted three-body problem

Beom Park*, Kathleen C. Howell

School of Aeronautics and Astronautics, Purdue University, 701 W. Stadium Ave, West Lafayette 47907, USA

Received 15 July 2024; received in revised form 2 January 2025; accepted 5 January 2025

Abstract

While the L₂ halo orbits as constructed in the Earth-Moon Circular Restricted Three-Body Problem (CR3BP) play an important role in future space exploration, the global behavior of the analogs within a Higher-Fidelity Ephemeris Model (HFEM) remains elusive. Leveraging a common numerical transition method from the CR3BP to the HFEM, the Earth-Moon L₂ halo family within the HFEM is characterized by producing multi-year HFEM counterparts. Two distinctive patterns emerge along the L₂ family: a nominal behavior in regions where analogs are well-defined and a transition-challenging behavior occurring in others. To gain deeper insights into the behavior of the HFEM analogs, the Elliptic Restricted Three-Body Problem (ER3BP) is employed. For the nominal behavior, the analysis demonstrates the formulation of HFEM solutions in the vicinity of the ER3BP structures. The transition-challenging behavior is demonstrated to be linked to fold bifurcations within the ER3BP continuation scheme, uncovering a potential dynamical reason for the challenges in transitioning from the CR3BP structures to the HFEM counterparts.

© 2025 COSPAR. Published by Elsevier B.V. All rights are reserved, including those for text and data mining, AI training, and similar technologies.

Keywords: CR3BP; ER3BP; Ephemeris transition

1. Introduction

Structures that exist within the context of Circular Restricted Three-Body Problem (CR3BP) are pivotal for supporting a variety of space mission concepts. Such structures include periodic and quasi-periodic orbits that offer trajectories with desired stability and geometry characteristics, enabling an efficient and strategic long-term presence throughout space. Within the Earth-Moon system, a prominent illustration is the 9:2 Near Rectilinear Halo Orbit (NRHO), known for its near-stability and access to the lunar vicinity (Zimovan-Spreen et al., 2020). It has been

designated as the baseline orbit for the NASA Gateway mission, aimed at reestablishing a sustainable human presence in cislunar space (Crusan et al., 2018). Similarly, within the context of the Sun-Earth system, NASA's Interstellar Mapping and Acceleration Probe (IMAP) (McComas et al., 2018) and the James Webb Space Telescope (JWST) (Clampin, 2008) missions leverage Sun-Earth L₁ and L₂ libration point orbits, respectively. In addition to these baseline trajectory design examples, transfer trajectory design is also facilitated by the preliminary analysis within the CR3BP dynamics (Wang et al., 2021; Muralidharan and Howell, 2023).

The structures supplied by the CR3BP framework necessitate the *transition* into Higher-Fidelity Ephemeris Model (HFEM) analogs suitable for flight, while preserving the desirable characteristics produced within the

* Corresponding author.

E-mail addresses: park1103@purdue.edu (B. Park), howell@purdue.edu (K.C. Howell).

Nomenclature

Glossaries

CR3BP	Circular Restricted Three-Body Problem
DFT	Discrete Fourier Transform
ER3BP	Elliptic Restricted Three-Body Problem

HFEM	Higher-Fidelity Ephemeris Model
PO	Periodic Orbit
QPO	Quasi-Periodic Orbit
NRHO	Near Rectilinear Halo Orbit

CR3BP. This transitioning process often entails the use of a differential corrections scheme, with the CR3BP trajectories serving as suitable initial guesses. [Dei Tos and Topputo \(2017\)](#) emphasizes the non-trivial aspect of this process, where the number of constraints is less than the number of free variables typically due to the loss of periodicity within the HFEM. The underconstrained nature of the problem renders it non-trivial and it is somewhat arbitrary to define and compute suitable counterparts within the HFEM. Various methods exist to supply the search direction for the corrector, with the minimum-norm Newton–Raphson method ([Davis et al., 2017; Dei Tos and Topputo, 2017; Zimovan-Spreen et al., 2020](#)) being commonly employed to construct trajectories that closely align with the original geometry constructed within the CR3BP. Optimizers are also employed to control the properties of the converged solutions within the HFEM ([Oguri et al., 2020](#)); however, the schemes rarely specifically leverage the underlying dynamical structures. Other factors such as the transition epoch, number of segments, and rotation schemes all potentially influence the solutions produced in the HFEM.

The identification and characterization of HFEM analogs typically entail navigating through arbitrary numerical aspects, yet insights from the evolution of the Hamiltonian structures deliver a better understanding of the HFEM solution behaviors. For the Earth-Moon system, [Gómez et al. \(2002\)](#) demonstrate that the Sun-Earth-Moon point-mass HFEM is approximated as a quasi-periodic Hamiltonian system with the Earth-Moon CR3BP perturbed by five distinct frequencies. [Jorba and Villanueva \(1997\)](#) prove the persistence of Hamiltonian structures under small perturbations; thus, provided that such structures exist, an HFEM analog may be effectively considered as an multi-dimensional Quasi-Periodic Orbit (QPO), inheriting frequencies from both the underlying CR3BP structures and the perturbations. Often, these HFEM analogs exist in proximity to the underlying CR3BP orbits. For instance, concerning the Earth-Moon L₂ halo orbits, [Lian et al. \(2013\)](#) as well as [Dei Tos and Topputo \(2017\)](#) illustrate the transition of a subset of the orbit family into HFEM quasi-periodic behavior by leveraging frequency information. Another example within this family pertains to the baseline trajectory for the Gateway mission, where [Zimovan-Spreen et al. \(2023\)](#) present a 20-year baseline

solution within the HFEM, leveraging a quasi-periodic motion evolving from the CR3BP halo orbit near the desired 9:2 synodic resonance ratio. These instances exemplify favorable scenarios where HFEM analogs are well-characterized, inheriting the motion of CR3BP structures. While the specific solutions depend on the numerical transitional process, they are expected to leverage the underlying basin of HFEM solutions, characterized by multi-dimensional QPOs in the vicinity of the CR3BP structures.

Conversely, an opposing scenario exists that underscores the arbitrary nature of the analogs, where characterizing the HFEM solution behaviors is challenging. Depending on the dynamical regimes, HFEM analogs are potentially located far from the original CR3BP solution; in such cases, the CR3BP structures may not serve as a desirable initial guess for the transition process. Furthermore, in the presence of non-negligible perturbations within the HFEM dynamics, QPOs within the HFEM may cease to exist. Within the Earth-Moon L₂ halo Periodic Orbit (PO) family, a subset near the synodic 3 : 1 resonance region potentially highlights such behavior, demonstrated by multiple previous investigations ([Davis et al., 2017; Boudad et al., 2022; Sanaga and Howell, 2024](#)). In this region, the transition behavior appears to be more random, where the HFEM solutions significantly depart from the underlying CR3BP orbits and are heavily dependent on the epoch. Also, multi-year solution behaviors are absent in the literature for this region, potentially suggesting a lack of the existence for the HFEM analogs altogether as multi-dimensional QPOs.

Within the previous context, the current investigation focuses on understanding the behaviors of the Earth-Moon CR3BP L₂ halo family as it transitions into HFEM counterparts. The selected region is notable for (1) its relevance to future space exploration, such as the Gateway mission, and (2) the recognized challenges in transition behavior near the 3:1 synodic resonance ratio. It is possible that other CR3BP structures across multiple systems display similar behavior where the Earth-Moon L₂ halo orbit simply provides a representative case. Thus, understanding the dynamical issues associated with such behavior potentially offers valuable insights into selecting CR3BP structures that exhibit favorable HFEM transition characteristics or devising mitigation strategies when transitioning is particularly challenging. These insights

ultimately contribute to a more versatile application of CR3BP structures for various space missions, and a more effective strategy to deliver suitable characteristics.

To facilitate the current investigation, an intermediate Hamiltonian system, the Elliptic Restricted Three-Body Problem (ER3BP), is employed to efficiently bridge the gap between the CR3BP and HFEM. The HFEM, as a time-dependent model, presents challenges in characterizing transition behaviors solely within the CR3BP. Conversely, working directly within the HFEM is intricate and sometimes obscure due to its complexity, where multiple perturbations governed by distinct frequencies simultaneously impact the transition process. Therefore, employing intermediate models that incorporate perturbations in ideal forms with a single frequency presents a practical alternative. Periodically perturbed Hamiltonian systems of this nature enable analysis of the evolution of CR3BP structures through numerical continuation and bifurcation analysis. While several intermediate models incorporate time-dependent perturbation components into the CR3BP (Andreu, 2003; Boudad et al., 2020; Sanaga and Howell, 2023; Villegas-Pinto et al., 2023; Liang et al., 2021; Peterson et al., 2023; Ferrari and Lavagna, 2018; Scheuerle et al., 2024), Park and Howell (2024) leverage an analytical formulation to select a desired dynamical model depending on the region of interest. They observe that the most significant source of perturbation within the Earth-Moon L₂ halo family in the HFEM is the time-varying distance between Earth and the Moon (pulsation). The Earth-Moon ER3BP interjects a realistic pulsation magnitude and appropriate frequency information, serving as a suitable intermediate model that approximates the most impactful time-dependent perturbations within the HFEM during the transition of Earth-Moon L₂ halo orbits. Note, however, that blindly incorporating the ER3BP as an intermediate step is not trivial; careful evaluation is required to yield dynamical insights within the ER3BP that feed forward to the numerical transition process from the CR3BP to HFEM.

The organization of the investigation unfolds as follows. Section 2 delves into a review of relevant dynamical models, including the CR3BP, ER3BP, and HFEM. Section 3 introduces the L₂ halo orbits within the CR3BP, and related structures within the CR3BP and ER3BP that originate from the halo structures. Section 4 outlines a consistent numerical transition scheme between the CR3BP and HFEM. With this approach, the HFEM analogs across the family are constructed methodically. To facilitate the analysis, the entire L₂ halo family is segmented into different regions based on two behaviors: nominal behavior, where HFEM analogs are well-defined, and transition-challenging behavior for scenarios where the analogs develop more randomly (if at all). Section 5 demonstrates that HFEM analogs corresponding to the nominal behavior formulate in close proximity to ER3BP structures, validated through the examination of hyperplane crossings and a spectral domain analysis. Subsequently, in Section 6,

bifurcation analysis within the ER3BP illustrates some likely dynamical causes for the transition-challenging behavior. A specific type of bifurcation, namely a fold bifurcation, is highlighted as a key metric in predicting regions within the cis-lunar space where establishing HFEM counterparts for CR3BP structures becomes particularly difficult. Lastly, concluding remarks are provided in Section 7.

2. Dynamical models

The current investigation employs three dynamical models: CR3BP, ER3BP, and HFEM. The differential equations for each model are reviewed, with common assumptions introduced. In all models, the spacecraft is reasonably assumed to deliver no influence on the celestial bodies' motion, and the celestial bodies are modeled as point masses. The gravitational parameter, the product of the gravitational constant and the mass of a celestial body, is denoted as $\tilde{\mu}$, defined consistent with JPL's ephemerides, DE440.bsp (Park et al., 2021). Subscripts E, M, and S indicate Earth, the Moon, and the Sun, respectively. For example, $\tilde{\mu}_E$ corresponds to the Earth's gravitational parameter.

2.1. Pulsating-rotating frame

The pulsating-rotating frame is employed for both model formulation and trajectory visualization throughout the current work. This frame is defined by three unit vectors: (1) \hat{x} is directed from the Earth to the Moon, (2) \hat{z} coincides with the angular momentum vector for motion of the celestial bodies, and (3) \hat{y} completes the dextral triad. The origin of the frame is the barycenter of the Earth and Moon. Regardless of the instantaneous dimensional Earth-Moon distance, the frame adopts a consistent nondimensional unit, where the nondimensional Earth-Moon distance is always unity. Within the frame, then, the Earth, Moon, and spacecraft are associated with following position vectors,

$$\vec{r}_E = -\mu \hat{x} \quad (1)$$

$$\vec{r}_M = (1 - \mu) \hat{x} \quad (2)$$

$$\vec{r}_s = x \hat{x} + y \hat{y} + z \hat{z}, \quad (3)$$

where μ denotes the mass ratio of the Earth and Moon defined as $\mu = \tilde{\mu}_M / (\tilde{\mu}_E + \tilde{\mu}_M)$. The subscripts E, M, and s denote the Earth, Moon, and spacecraft, respectively. Note that the Earth and Moon position vectors are fixed within the rotating frame along the \hat{x} axis, separated by a unit nondimensional distance. The pulsating-rotating frame is also denoted as "rotating frame" in the current investigation.

2.2. Circular restricted three-body problem (CR3BP)

The CR3BP is comprised of the Earth, the Moon, and the spacecraft. In an inertial frame, the primaries (the

Earth and the Moon) orbit their mutual barycenter in circular paths with a radius of constant l_* , denoted the characteristic length. The characteristic time $t_* = \sqrt{l_*^3/(\tilde{\mu}_E + \tilde{\mu}_M)}$, is then defined accordingly. Within the rotating frame, the spacecraft motion is governed by following nondimensional equations of motion,

$$\frac{d^2\vec{r}_s}{dt^2} = -2\hat{z} \times \frac{d\vec{r}_s}{dt} + \nabla\Omega_C, \quad (4)$$

where the independent variable for the CR3BP is denoted as t , representing the nondimensional time. The pseudo-potential function in the CR3BP is defined by $\Omega_C = (x^2 + y^2)/2 + \Omega$, where $\Omega = (1 - \mu)/r_{Es} + \mu/r_{Ms}$, and r_{Es} and r_{Ms} represents the nondimensional distance between the Earth and the spacecraft and between the Moon and the spacecraft, respectively. The cross product is represented by the symbol \times .

2.3. Elliptic restricted three-body problem (ER3BP)

The ER3BP incorporates conic motion for the primaries. The true anomaly of the Moon with respect to Earth is represented by f , serving as the independent variable in the ER3BP. The eccentricity of the conic orbit for the primaries is denoted as e . The motion of the spacecraft is governed by the following equations within the pulsating-rotating frame,

$$\frac{d^2\vec{r}_s}{df^2} = -2\hat{z} \times \frac{d\vec{r}_s}{df} + \nabla\Omega_E. \quad (5)$$

Here, Ω_E is the pseudo-potential function for the ER3BP, evaluated as $\Omega_E = \frac{1}{1+e\cos f}\Omega_C - \frac{e\cos f}{1+e\cos f} \cdot \frac{z^2}{2}$. Note that when e is zero, the ER3BP reduces to the CR3BP and f becomes equivalent to nondimensional t . While various values for e are utilized, Park and Howell (2024) suggest that values between 0.05 and 0.055 typically represent realistic Earth-Moon motion. In the current work, $e = 0.055$ is selected to reflect a desirable realistic value, denoted as e_d . The ER3BP is a periodically perturbed Hamiltonian system with a period of 2π with respect to the true anomaly, f .

2.4. Higher-Fidelity Ephemeris Model (HFEM)

In the current work, the HFEM incorporates three celestial bodies: the Earth, the Moon, and the Sun. The ephemerides for these bodies are accessed from DE440.bsp. The spacecraft motion within the Moon-centered ECLIPJ2000 inertial frame, under the gravitational influence of these celestial bodies, is described by the following dimensional equations of motion,

$$\frac{d^2\vec{R}_s}{dT^2} = -\frac{\tilde{\mu}_M}{R_s^3}\vec{R}_s + \sum_{p=E,S}\tilde{\mu}_i\left(\frac{\vec{R}_{sp}}{R_{sp}^3} - \frac{\vec{R}_{Mp}}{R_{Mp}^3}\right), \quad (6)$$

where \vec{R}_s denotes the dimensional, inertial position of the spacecraft with respect to the Moon, where the magnitude

is labelled R_s . The independent variable T represents the dimensional time in seconds that governs the HFEM dynamics. The perturbing bodies are represented as p , where only Earth (E) and the Sun (S) are included in this analysis. Then, \vec{R}_{sp} and \vec{R}_{Mp} denote the position vectors directed from the spacecraft and the Moon to the perturbing body, respectively. To visualize the HFEM trajectories within the rotating frame, it is necessary to properly rotate and nondimensionalize the inertial state \vec{R}_s into \vec{r}_s . This process is accomplished by leveraging the following relationship,

$$\vec{R}_s = \vec{R}_B + R_{EM}\mathbf{C}\vec{r}_s, \quad (7)$$

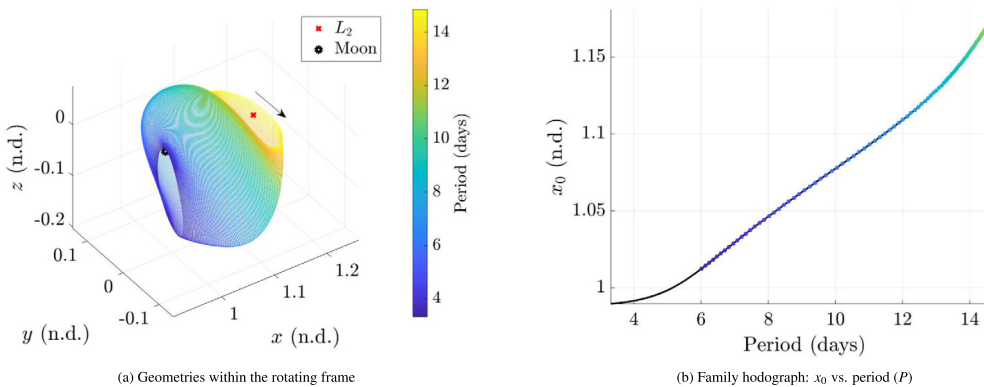
where \vec{R}_B corresponds to the inertial position of the Earth-Moon barycenter with respect to the Moon, and \mathbf{C} is a direction cosine matrix with the instantaneous directions of \hat{x}, \hat{y} and \hat{z} constructed from the ephemerides data. These directions are evaluated as $\hat{x} = \vec{R}_{EM}/R_{EM}$, $\hat{z} = \vec{H}/H$, where $\vec{H} = \vec{R}_{EM} \times d\vec{R}_{EM}/dT$, and $\hat{y} = \hat{z} \times \hat{x}$. Note that \vec{R}_B and \mathbf{C} are functions of the dimensional time T and require retrieval of instantaneous ephemerides quantities.

3. Earth-Moon L₂ Halo Orbits and Related Structures within the CR3BP and ER3BP

The focus of the current investigation is L₂ halo orbits, as defined for the Earth-Moon system. The halos orbits, nearby CR3BP structures and the corresponding ER3BP counterparts are reviewed. Structures of interest are POs and QPOs within the CR3BP and ER3BP; these Hamiltonian structures allow an angular representation of the structures that aid analysis.

3.1. CR3BP L₂ Halo periodic orbits

The L₂ halo family of orbits emanates from the planar L₂ Lyapunov orbit family through a pitchfork bifurcation, where the southern and northern halo families exist as mirror configurations across the $\hat{x} - \hat{y}$ plane within the rotating frame. The current investigation focuses on the southern family for its relevance in the near future cislunar space exploration, e.g., the 9:2 southern Near Rectilinear Halo Orbit (NRHO). A representative set of orbits from the Earth-Moon L₂ southern halo family is illustrated in the rotating frame in Fig. 1(a). The CR3BP POs are diffeomorphic to topological circles. Thus, any state on a PO is parameterized by a single angle, also denoted as the longitudinal angle, θ_P , that evolves linearly with the independent variable and an associated frequency v_P . The subscript 0 denotes the zero longitudinal angle, $\theta_{P,0} = 0$ rad, referenced at the apolune of each orbit. All the angles are represented in radians (rad) for consistency. The plotted orbits in Fig. 1(a) are a subset of the family that remain above the lunar radius. Fig. 1(b) illustrates the hodograph for the x position at the apolune location, i.e., x_0 , versus the period of the orbit in days. For dimensionalization of time,

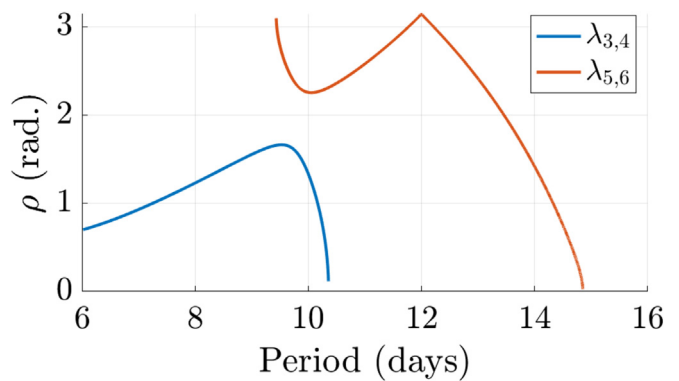
Fig. 1. Earth-Moon L₂ southern halo family.

$t_* \approx 375699$ seconds is multiplied with the non-dimensional period. Note that the Earth-Moon L₂ halo family admits a monotonic evolution of the period. Thus, in the current investigation, the period of the orbit is adopted as the parameter to specify each member along the family, typically visualized on the horizontal axis as displayed in Fig. 1(b).

3.2. Nearby CR3BP L₂ higher-period periodic orbits and quasi-periodic orbits

Stability information for the CR3BP PO is reviewed here. The PO within the CR3BP is also represented by a constant-time mapping function, $\vec{\psi} : \mathbb{R}^6 \rightarrow \mathbb{R}^6$, that maps a fixed point to itself after one period, P . Representing the fixed point as $\vec{s} \in \mathbb{R}^6$, consisting of the position and velocity of the spacecraft as evaluated within the rotating frame, i.e., \vec{r}_s and $\dot{\vec{r}}_s = d\vec{r}_s/dt$, respectively, $\vec{\psi}(\vec{s}) = \vec{s}$. The monodromy matrix is accordingly defined as $\mathbf{M} := \frac{\partial \vec{\psi}}{\partial \vec{s}}$. The monodromy matrix contains the linear stability information for the PO and provides the information for any nearby structures. As the CR3BP is a Hamiltonian system, the six eigenvalues for \mathbf{M} occur in three reciprocal pairs. Additionally, since the CR3BP is an autonomous system and the CR3BP POs exist in families with varying periods, \mathbf{M} produces a trivial eigenvalue pair, $\lambda_{1,2} = 1$. The geometric multiplicity for this eigenvalue is 1, thus, \mathbf{M} for CR3BP POs is always defective. The normal eigenvector for the trivial pair corresponds to the along-orbit direction, and the generalized eigenvector is associated with the family tangent direction (Wiesel and Pohlen, 1994; Williams et al., 2023). Two other reciprocal pairs are denoted as $\lambda_{3,4}$ and $\lambda_{5,6}$.

When \mathbf{M} admits a linear center subspace, $\lambda_{3,4}$ or $\lambda_{5,6}$ (or both) reside on the unit circle within the complex plane. These center eigenvalues for POs along the L₂ halo family that remain above the lunar radius are illustrated in Fig. 2, where the vertical axis visualizes the rotation number constructed as,

Fig. 2. The rotation number (ρ) along the family.

$$\rho = \arccos(\operatorname{Re}(\lambda)), \quad (8)$$

with $\rho \in [0, \pi]$. Note that a slightly different definition is employed in Lujan and Scheeres (2022) where ρ is defined between 0 and 2π . As the eigenvalues occur as conjugate pairs, the definition within the range of $\rho \in [0, \pi]$ also covers all possibilities. From Fig. 2, note that for a subset of the family near $P = 10$ days, both pairs $\lambda_{3,4}$ and $\lambda_{5,6}$ reside on the unit circle. For the given range of periods, the family admits at least one pair of eigenvalues on the unit circle (For the range $P < 6$ days, refer to Lujan and Scheeres (2022) as well as Zimovan-Spreen et al. (2020)). In a linear sense, ρ signifies the rotated angle within the linear center subspace for a given perturbation within the subspace after one period, P . The linear center subspace is tangent to the nonlinear center manifolds, potentially leading into nearby CR3BP higher-period POs or the QPOs.

When ρ is in resonance with 2π , or, a rational multiple of 2π , the CR3BP PO undergoes a bifurcation leading to the formation of a higher-period PO family, also denoted period-multiplying bifurcations. In such instances, there exist positive coprime integers p and q satisfying $p : q = 2\pi : \rho$. An illustrative example appears in Fig. 3, depicting the period-tripling bifurcation from a location where $\rho = 2\pi/3$. In Fig. 3(a), the L₂ halo family is represented in black, with the horizontal axis corresponding to

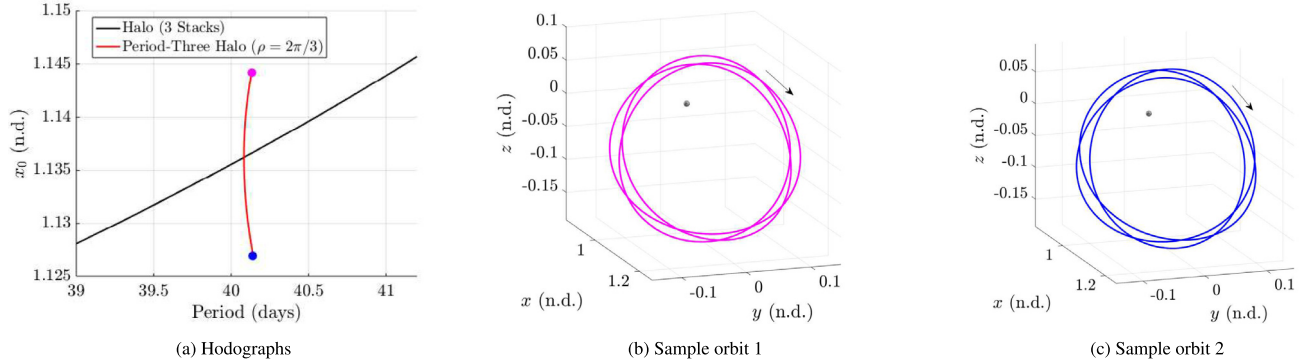
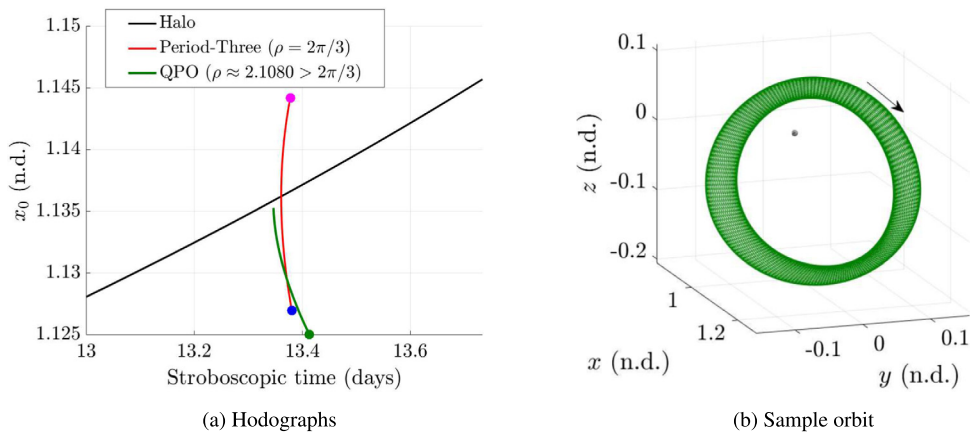


Fig. 3. Higher-period halo example: period-tripling bifurcation.

the periods of the orbits in days. To depict the intersection with the period-tripling family, the periods of the halo orbits are multiplied by three. Through the period-tripling bifurcation, a new family emerges from the original orbit where $\rho = 2\pi/3$, portrayed in red. Fig. 3(b) and (c) showcase two sample orbits constructed at either end of the red hodograph from Fig. 3(a). It is essential to observe that, although the new family evolves with different values of period, it maintains the original rotation number, i.e., $\rho = 2\pi/3$. This behavior is evident from the fact that the orbit geometries both involve three distinct lobes. Therefore, higher-period periodic orbit families are regarded as constant ρ branches within the CR3BP in the present investigation.

When ρ is not in resonance with 2π , or when $2\pi/\rho$ is an irrational number, the CR3BP POs undergo bifurcations leading to the formation of QPOs. Each center mode depicted in Fig. 2 yields a two-parameter QPO family, where P represents the period of the underlying halo orbit, and ρ governs the rotation number per stroboscopic mapping time, i.e., P . It is noteworthy that the family is Cantor; specifically, when ρ is in resonance with 2π rad, the QPOs collapse to higher-period periodic orbits. While various strategies exist to define a one-parameter family or branch for QPOs (Olikara, 2016), a constant ρ QPO branch is analogous to a higher-period PO branch. The QPOs are

diffeomorphic to topological tori and involve two angular variables for parameterization. The rotation number ρ signifies the change in the latitudinal angle per stroboscopic time P , i.e., one cycle of the longitudinal angle. Notably, the longitudinal angle is associated with the underlying CR3BP PO, while the latitudinal angle originates from the center mode of the periodic orbit within the CR3BP. An example is included in Fig. 4. Fig. 4(a) illustrates the hodograph for the QPO branch with fixed $\rho \approx 2.1080$ rad. This number is slightly larger than the nearby resonance ratio, $\rho = 2\pi/3$ rad, for which the QPO branch degenerates into the period-three PO family. Note that these hodographs represent sample continuation results and do not signify the end of the families. The red curve within Fig. 4(a) represents the same period-three branch as illustrated in Fig. 3(a). The horizontal axis in Fig. 4(a) utilizes stroboscopic time instead of the period of the orbit to accommodate both the period-multiplied POs and QPOs within the same plot. For the period-three halo orbit, the stroboscopic time is defined as the period of the orbit divided by three. One sample orbit is illustrated in Fig. 4(b), corresponding to the green circle from Fig. 4(a). The significance of these nearby CR3BP structures is demonstrated later in Section 6, where the continuation process within the ER3BP often links with them.

Fig. 4. Quasi-periodic orbit example: $\rho \approx 2.1080$ rad.

3.3. ER3BP L_2 Halo counterparts: periodic orbits and quasi-periodic orbits

Given that the ER3BP is a periodically perturbed system, the CR3BP POs typically transform into ER3BP POs and QPOs with a non-zero eccentricity. Thus, another rotation angle is introduced as,

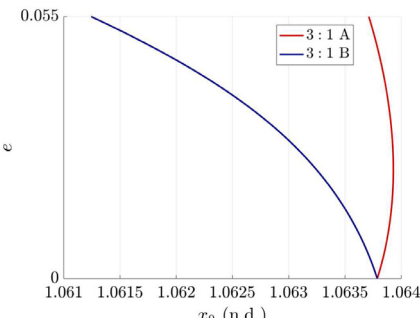
$$\rho_E = P, \quad (9)$$

that quantifies the change in phase (representing the latitudinal angle within the ER3BP structures) per stroboscopic mapping time, P . Note that this angle is distinct from ρ as defined in the center subspace of the CR3BP PO. However, there is a possibility that the two are offset by $2k\pi$ for an integer k , a property discussed further in Section 6.2.2. Similar to the evolution of CR3BP higher-period POs and QPOs, the transformation into ER3BP POs and QPOs is influenced by the resonance of ρ_E with respect to 2π .

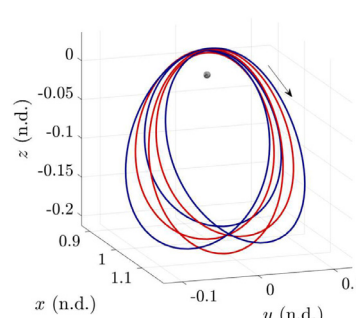
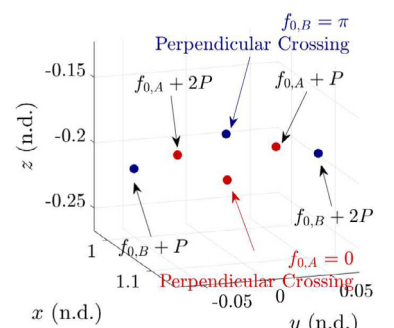
3.3.1. ER3BP POs

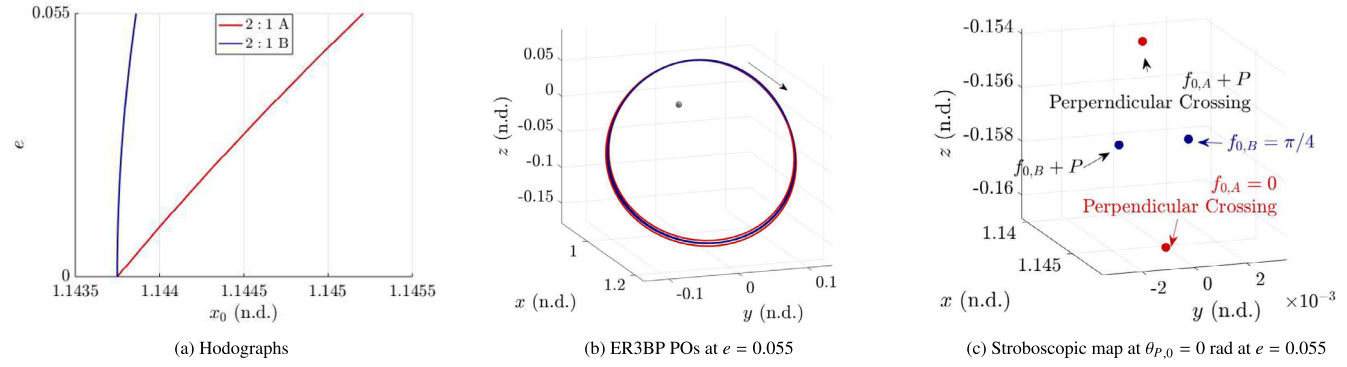
In instances where ρ_E is in resonance with 2π , the CR3BP POs evolve into the ER3BP POs. As the ER3BP is a periodically perturbed system with a period of 2π with respect to the true anomaly, f , the period of the orbit must be commensurate with the period of the dynamics to allow a PO. The ER3BP POs in this analysis are characterized by the rational ratio $p : q$, where $p : q = 2\pi : P$, with p and q being positive coprime integers. For every $p : q$ ratio, multiple authors (Ferrari and Lavagna, 2018; Campagnola et al., 2008; Peng and Xu, 2015) numerically observe that two counterparts generally exist that satisfy the mirror configuration. The trivial eigenvalue pair from the CR3BP PO, i.e., $\lambda_{1,2} = 1$, distinctively bifurcates into saddle and center pairs for each counterpart as first observed by Campagnola et al. (2008). The loss of the trivial pair at $e = 0$ is intricately tied to the time-dependent nature of the dynamics. Consequently, the ER3BP POs exist as island solutions at a fixed eccentricity value. This property occurs in contrast to the CR3BP POs that exist in families with varying periods. Rather, the ER3BP POs exist as “families” with varying eccentricity levels, i.e., the model itself is required to shift to admit a nearby PO.

Two ER3BP PO counterparts are associated with different phasing information, f_0 . Recall that the subscript 0 refers to the zero longitudinal angle, $\theta_{P,0} = 0$ rad, referenced at the apolune of the original CR3BP POs. For p that is odd, e.g., $p = 3$, two counterparts exist for $f_0 = 0$ rad and $f_0 = \pi$ rad, denoted as counterpart ‘A’ and ‘B’, respectively. An example appears in Fig. 5 for $p : q = 3 : 1$, where $\rho_E = 2\pi/3$ rad for $P = 2\pi/3$ n.d., or, approximately 9.1 days. Note that as the e value for the ER3BP increases, the equivalent dimensional period of the underlying orbit may indeed shift; P references the original CR3BP value at $e = 0$, where f reduces to t . The hodographs for two counterparts are plotted in Fig. 5(a) with the eccentricity as a function of the x_0 location (apolune) of the orbit. Two counterparts at $e = 0.055$ are visualized within the rotating frame in Fig. 5(b). The crossings from the two counterparts at the stroboscopic map are plotted in Fig. 5(c). The counterpart ‘A’ (red) admits a perpendicular crossing at $f_0 = 0$ rad, i.e., $y = dx/df = dz/df = 0$. Then, the subsequent crossings after P and $2P$ are marked with red circles. Similarly, the counterpart ‘B’ (blue) initiates from another different perpendicular crossing at $f_0 = \pi$ rad and then marks distinct crossings after each return. Note that $f_{0,A} + k \cdot P$ with an integer $k, 0 \leq k \leq p - 1$, corresponds to the latitudinal angle for the ER3BP POs at the stroboscopic map at $\theta_{P,0}$. Crossings from two counterparts more densely fill $[0, 2\pi)$ for larger p values. For an even number p , counterpart ‘A’ is associated with $f_0 = 0$ rad, but counterpart ‘B’ is associated with $f_0 = \pi/2$ rad. An example is included for $p : q = 2 : 1$ in Fig. 6. Note that, for the stroboscopic map at $\theta = 0$ rad., i.e., apolune, the two perpendicular crossings originate solely from the counterpart ‘A’. Also $f_0 = \pi$ rad connects back to the counterpart ‘A’ and does not supply an additional counterpart. Rather, counterpart ‘B’ is offset by $\pi/2$ rad in f_0 at the stroboscopic map; this counterpart results in two perpendicular crossings near perilune. Thus, while general characteristics for the two counterparts remain the same, i.e., both counterparts gradually fill the latitudinal angle curve with an offset initial f_0 value, the computational process slightly differs for an odd or even p . The computational scheme in the current investigation



(a) Hodographs

(b) ER3BP POs at $e = 0.055$ (c) Stroboscopic map at $\theta_{P,0} = 0$ rad at $e = 0.055$ Fig. 5. ER3BP PO example with an odd number p ($p : q = 3 : 1$).

Fig. 6. ER3BP PO example with an even number p ($p : q = 2 : 1$).

leverages a perpendicular crossing at the rotating frame $\hat{x} - \hat{z}$ plane. When p is odd, the apolune state ($\theta_P = 0$ rad) along the CR3BP PO is leveraged to produce both counterparts by assigning different f_0 values. For an even number p , to utilize the perpendicular crossing scheme, the perilune state ($\theta_P = \pi$ rad) is leveraged, initialized with zero true anomaly ($f_0 = 0$), to yield counterpart ‘B’. From Eq. (5), note that negative eccentricity in the ER3BP dynamics results in a phase shift by $\Delta f = \pi$ rad due to the cosine function that appears in the equations of motion. Thus, two counterparts for an odd number p are linked via continuation in positive and negative eccentricity directions, but they are not connected for an even number p . In the current work, for a consistent representation, only a positive range of e is employed, and states at $\theta_{P,0} = 0$ rad are then used to plot hodographs. Refer to Peng and Xu (2015) for more information on the construction of the two ER3BP PO counterparts. For reference, the initial state and true anomaly corresponding to two counterparts for 3:1 and 2:1 ER3BP POs are included in Table 1, constructed at the end of hodographs with $e = 0.055$.

3.3.2. ER3BP QPOs

When $P/2\pi$ is an irrational number, the CR3BP POs are guaranteed to evolve into the ER3BP QPOs for a sufficiently small eccentricity value (Jorba and Villanueva, 1997). The ER3BP QPOs inherit the frequency of the underlying CR3BP PO and the frequency of the perturbation. While analytical boundaries for the existence of QPOs

remain an unresolved issue, numerical algorithms are leveraged to approximate them. In the current work, an algorithm developed by Gómez and Mondelo (2001) as well as Olikara and Scheeres (2012) (GMOS) is employed. This algorithm formulates a two-point boundary problem that numerically targets the *invariance condition*. For a fixed longitudinal angle at $\theta_{P,0} = 0$ rad, multiple initial conditions associated with different initial true anomalies are sampled; these initial conditions approximate the smooth, periodic invariant curve. Then, after one stroboscopic mapping time P , the final state along each trajectory remains on the same invariant curve but is rotated by ρ_E . More information on the algorithm is included in the B that refers to the methodology by Olikara and Scheeres (2012).

Similar to the CR3BP QPOs discussed in Section 3.2, the ER3BP QPOs generally exist as a two-parameter family governed by the underlying period P , or equivalently ρ_E , and the eccentricity e . Two continuation strategies are typically employed to map out the members of this two-parameter family (McCarthy, 2022). The first method involves continuing from each CR3BP PO and varying the model parameter e . An alternative continuation strategy adopts an evolution in ρ_E . While both approaches provide complementary search directions to fully map out the two-parameter family, the continuation in e is predominantly employed in the current work due to certain benefits. First, for the ER3BP POs, continuation in the rotation number is challenging, as each PO family within

Table 1

Initial state and true anomaly for the ER3BP POs at $e = 0.055$ from Figs. 5 and 6

	3:1 A	3:1 B	2:1 A	2:1 B
x_0 (n.d.)	1.063711073613819	1.061243374335881	1.145207142692959	1.042729354452091
y_0 (n.d.)	0	0	0	0
z_0 (n.d.)	-0.212478670582939	-0.177892876821336	-0.160871833424495	0.074549237288375
$\left(\frac{dx}{dt}\right)_0$ (n.d.)	0	0	0	0
$\left(\frac{dy}{dt}\right)_0$ (n.d.)	-0.163095487396061	-0.206825448422955	-0.220905042713801	0.388471995882814
$\left(\frac{dz}{dt}\right)_0$ (n.d.)	0	0	0	0
f_0 (rad)	0	π	0	0

the ER3BP exists at discrete ρ_E values associated with different $p : q$ ratios. Rather, it is typical to vary the eccentricity for the PO continuation process. Employing the same continuation direction in the QPO computation, it is possible to compare the numerical results for both types of structures as demonstrated later in Section 6.2. Moreover, the ER3BP QPOs collapse to ER3BP POs for ρ_E values that are in resonance with 2π . A larger boundary in ρ_E exists near each resonant ratio, as noted by Olikara et al. (2016), due to the center mode for one counterpart in $p : q$ CR3BP POs (recall that $\lambda_{1,2}$ from the CR3BP evolve onto saddle and center pairs for each counterpart) within the ER3BP. While it is possible to numerically detect and jump these resonance gaps (Henry et al., 2023), the continuation in eccentricity is less susceptible to this challenge and is considered advantageous. A continuation example from an ER3BP QPO family is plotted in Fig. 7 for $P \approx 14.8$ days, corresponding to $\rho_E \approx 3.4$ rad. Note that 51 nodes are incorporated here to discretely approximate the invariant curve, as visualized in Fig. 7(c). Additionally, a single QPO covers the entire range of f values at the stroboscopic map; thus, continuation in negative eccentricity does not generate different solutions, and $e > 0$ is leveraged, similar to the ER3BP PO computation.

4. Multi-year HFEM counterparts for L₂ Halo Orbits

4.1. Multi-year HFEM ballistic counterparts: “Unraveling” quasi-periodic structures

In general, each CR3BP L_2 halo orbit ultimately yields infinite HFEM counterparts, with the specifics of the individual solutions dependent on the particular numerical transition process. This trait arises due to the underconstrained nature of the problem (Dei Tos and Topputo, 2017); while the original CR3BP halo orbits are periodic, this property is not preserved within the HFEM. Consequently, the numerical targeting problem becomes underconstrained, requiring the specification of a search direction. The freedom to select this direction leads to the

generation of multiple, infinite HFEM analogs from the CR3BP POs.

Despite the varying details of the solutions produced through a transition process, observable patterns emerge for sufficiently long HFEM counterparts. Gómez et al. (2002) provide relevant background on the nature of HFEM analogs, demonstrating that the Sun-Earth-Moon HFEM dynamics are reasonably approximated in terms of a quasi-periodic dynamical model. In addition to the CR3BP dynamics, the HFEM model includes a set of perturbations governed by at least five distinct frequencies. These quasi-periodic perturbations enable the evolution of the CR3BP POs into higher-dimensional quasi-periodic structures within the HFEM. Although the exact construction of higher-dimensional quasi-periodic structures remains challenging, as demonstrated by McCarthy (2022), Lian et al. (2013) observe that over a sufficiently long time horizon, spanning several decades, the HFEM analogs reveal the existence of quasi-periodic structures governed by multiple frequencies. In light of this context, the objective here is the investigation of the behavior of multi-year HFEM ballistic analogs. These multi-year counterparts are adequate for characterizing HFEM behavior, as they offer a clearer representation of the quasi-periodic nature, reducing the impact of randomness from the numerical process that is observed in short-term solutions.

4.2. Numerical transition process and initial results for HFEM analogs

The numerical transition process in this investigation focuses on determining multi-year HFEM counterparts originating from the CR3BP L_2 halo orbits. The key strategy to accomplish the evolution is to *stack* multiple revolutions of the CR3BP POs, forming longer trajectories that serve as the initial guess for the transition process. This approach relies on the assumption that quasi-periodic structures within the context of the HFEM exist in the vicinity of the stacked orbits, offering desirable starting points. To begin the transition process, the stacked trajectories are discretized into multiple patchpoint states.

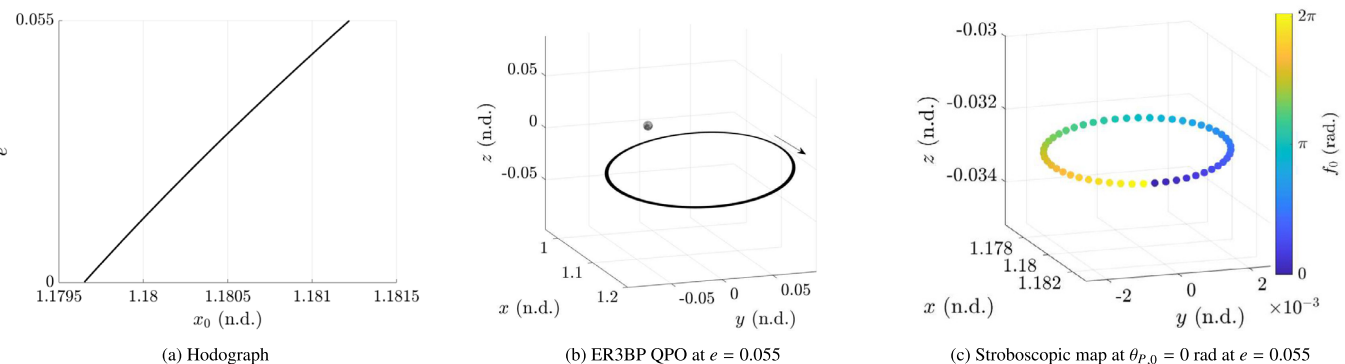


Fig. 7. ER3BP QPO example with $P \approx 14.8$ days.

A targeting problem is then formulated, where the patchpoint states are repositioned for continuity under HFEM dynamics. This practice is common and appears in multiple references, including Oguri et al. (2020) and Bosanac et al. (2018). As previously mentioned, the loss of the periodicity constraint in the HFEM leaves a crucial gap, i.e., no scheme to specify the search direction during the targeting process. One possible alternative is defining a cost function and pairing it with an optimizer to determine the search direction that optimizes the cost. This cost function may incorporate, for instance, the desired characteristics of the original solutions, such as the apse angle and time-of-flight. However, in the current investigation, a minimum-norm approach is preferred over an optimizer due to its computational efficiency. The minimum-norm solver aims to minimize the change from the previous guess at each step in the targeting scheme, reducing the deviation from the initial guess delivered via the CR3BP.

The numerical formulation leveraging a minimum-norm approach is elaborated here, drawing similarities with the formulation in Bosanac et al. (2018). Multiple CR3BP halo orbits over a desired horizon time are stacked and discretized. The i -th patchpoint state along the stack of the CR3BP POs is denoted as $\vec{r}_{s,i}$ and $\dot{\vec{r}}_{s,i} = d\vec{r}_{s,i}/dt$ for position and velocity as observed from the rotating frame, respectively. The total number of patchpoints is represented by m , where $1 \leq i \leq m$. The independent variable associated with the i -th patchpoint is denoted t_i and arranged in increasing order of time. For the reference index, denoted as subscript “ref”, the time is initialized as zero, i.e., $t_{\text{ref}} = 0$. In the current investigation, the reference index is evaluated as $\text{ref} = (m + 1)/2$, corresponding to the “innermost” patchpoint from the CR3BP stack. The next step transforms the CR3BP states and time variables at the patchpoints into the HFEM dimensional quantities. For position and velocity rotation and dimensionalization, Eq. (7) is leveraged to retrieve initial guesses for $\vec{R}_{s,i}$ and $\vec{R}_{s,i}' = d\vec{R}_{s,i}/dT$, respectively. For a more detailed discussion on the derivative of Eq. (7), refer to Park and Howell (2024). The initial guess for the HFEM independent variable T_i , corresponding to t_i , is retrieved as,

$$T_i = \int_{t_{\text{ref}}}^{t_i} \sqrt{\frac{R_{EM}^3(T)}{\mu_E + \mu_S}} dt, \quad (10)$$

where R_{EM} corresponds to the instantaneous dimensional Earth-Moon distance. Note that T_i is the dimensional time measured from the user-specified fixed reference epoch, JD_{fix} ; thus, $T_{\text{ref}} = 0$. The integration time between the i -th and $(i+1)$ -th patchpoints is determined as $\Delta T_i = T_{i+1} - T_i$ for $1 \leq i \leq m-1$. The epoch associated with each patchpoint state is denoted $JD_i = JD_{\text{ref}} + T_i/(3600 \cdot 24)$, representing the Julian Date. Using this formulation, the initial guess for the multiple shooting algorithm is constructed as,

$$\vec{X} = \left[\vec{R}_{s,1}^{\top}, \vec{R}_{s,1}'^{\top}, \dots, \vec{R}_{s,m}^{\top}, \vec{R}_{s,m}'^{\top}, \Delta T_1, \dots, \Delta T_{m-1}, JD_1, \dots, JD_m \right]^{\top}, \quad (11)$$

where decomposing T_i into the propagation time (ΔT) and epoch (JD) often results in a more robust configuration for the corrections process. A transpose of a vector or matrix is denoted as a superscript \top . Thus, the constraint is then formulated as,

$$\vec{F} = \left[\vec{F}_{\text{state}}^{\top}, \vec{F}_{\text{epoch}}^{\top}, \vec{F}_{\text{ref}}^{\top} \right]^{\top}. \quad (12)$$

The subscript “state” denotes the state continuity, ensuring that the propagated states from the i -th patchpoint coincide with the $(i+1)$ -th patchpoint state for both position and velocity components. This formulation corresponds to a forward propagation, where backward propagation in time is also leveraged as appropriate (Davis et al., 2017). Similarly, the subscript “epoch” represents the following epoch continuity constraint, $JD_{i+1} = JD_i + \Delta T_i/(3600 \cdot 24)$. The “ref” subscript corresponds to the reference epoch constraint, where $JD_{\text{ref}} = JD_{\text{fix}}$. Under this formulation, the length of \vec{X} is $8m - 1$, whereas the length of \vec{F} is $7m - 6$, illustrating the underconstrained nature of the problem. Here, the minimum norm approach specifies the search direction through the following iterative update steps,

$$\vec{X}_{j+1} = \vec{X}_j - \mathbf{J}^{\top}(\mathbf{J}\mathbf{J}^{\top})^{-1}\vec{F}_j, \quad (13)$$

where \vec{X}_{j+1} represents the updated solution at the $(j+1)$ -th iteration, while \vec{X}_j is the current solution at the j -th iteration. The matrix \mathbf{J} is the Jacobian of the constraint vector \vec{F} with respect to the free variable vector \vec{X} , evaluated at \vec{X}_j . Note that the number of columns in the Jacobian matrix is greater than the number of rows. Consequently, the minimum norm approach allows the determination of a search direction that minimizes the step size at each iteration. Specifically, the strategy aims to minimize the norm of $\Delta X_j := \vec{X}_{j+1} - \vec{X}_j$ while satisfying the constraint $\mathbf{J}\Delta X_j = -\vec{F}_j$. Although the formulation in Eq. (13) is presented in dimensional units for illustrative purposes, it is common practice to nondimensionalize the variables using the constant characteristic quantities from the CR3BP, i.e., l_* (length) and t_* (time), to maintain consistent scaling properties. This transition scheme is labelled “direct,” signifying that no intermediate steps are involved between the CR3BP POs and the HFEM solutions.

Consistent with the direct transition strategy, the CR3BP halo orbits visualized in Fig. 1(a) are transitioned to the HFEM. The numerical formulation involves employing five patchpoints per CR3BP orbit, with a reference epoch on $JD_{\text{fix}} = 09/23/2023$. Convergence is achieved when the non-dimensional l^2 norm of \vec{F} falls below a tolerance value $1 \cdot 10^{-10}$, ensuring reasonably

accurate solutions. Initially, constructing 20-year analogs is attempted, representing the maximum horizon time explored in this investigation. However, when the targeter fails to converge within a specified maximum number of iterations, selected as 30, the horizon time is reduced. Consequently, five different horizon times are investigated, progressing from 20 years down to 10 years, 5 years, 3 years, and finally 1 year. While there are no fixed criteria to define "multi-year" counterparts, the Saros period, approximately 18.029 years, spans some of the most relevant periods reflected in the Earth-Moon system with near integer revolutions of synodic, anomalistic and draconic months (Andreu, 1998). Therefore, 20 years is selected as the maximum horizon time for this investigation over which the HFEM solutions are expected to display quasi-periodic behavior. The results from this formulation using a direct approach to transition the CR3BP halo orbits to the HFEM are visually represented in Fig. 8, where the vertical axis represents the horizon time achieved through the numerical process. The horizontal axis is defined in terms of the period, P , for the CR3BP halo orbits that are employed for the initial guesses. For a significant number of cases, the transition process successfully yields multi-year HFEM analogs (**nominal behavior**), with a predominant horizon time equal to 20 years, evident from the data points clustered around the 20-year mark on the vertical axis. However, note that certain counterparts fall within an "intermediate" region associated with a **transition-challenging behavior**, where convergence leads to lower horizon times or failure to converge even over the minimum horizon time of one year. These specific counterparts are denoted in orange within the figure, as their horizon times drastically decrease below one year.

Based on the observed characteristics, the halo family of orbits is divided into three distinct regions: the (1) NRHO Region ($P < 8.6$ days), (2) Interface Region ($8.6 < P < 11.0$ days), and (3) Regular Halo Region ($P > 11.0$ days). Sample analogs from each region are illustrated in Fig. 9. Notably, the HFEM counterparts within the NRHO and Regular Halo Regions closely align with the initial guesses from the CR3BP as viewed in the rotating frame and display the defined **nominal behavior**. However, the Interface Region exhibits significantly dispersed geometries corresponding to the **transition-challenging behavior**. This observation is consistent with Davis et al. (2017) as well as Sanaga and Howell (2024), who note that

the HFEM analogs are associated with "less-periodic" behavior for a subset of L_2 halo orbits.

Building upon these observations, the transition-challenging behavior, a key trait for the Interface Region, manifests two features: (1) a significant drop in the horizon of the HFEM solutions, and (2) even when an analog is successfully constructed, the geometries are associated with more dispersed behavior as viewed within the rotating frame. It is deduced that the initial guess from the CR3BP POs do not serve as suitable initial guess for the transition process based on the given numerical formulation, provided that the goal is to retrieve a sufficiently long ballistic trajectory that maintains the original solution characteristics from the CR3BP. One possible dynamical explanation is that the quasi-periodic structures that exist within the HFEM deviate significantly from the CR3BP POs. Moreover, under the HFEM dynamics, the underlying quasi-periodic structures may break down, challenging the construction of bounded solutions for multiple years. Note, however, that the specific results visualized in Fig. 8 may vary depending on the specifics of the numerical formulation employed, including but not limited to, (1) patchpoint placement schemes, (2) propagation directions, (3) baseline epochs, and (4) more refined search directions and step sizes. Thus, the results serve as an illustrative experiment to demonstrate the generic trend observed in transitioning the CR3BP halos into HFEM analogs.

4.3. Continuation scheme and updated results for the interface region

Within the Interface Region, the quasi-periodic structures in the HFEM, even if they exist, are potentially located "far" from the CR3BP POs. Indeed, the behaviors as observed in Figs. 8 and Fig. 9(b) are likely related to both the numerical and dynamical factors. While it is obviously impossible to attempt "all possible cases," exploring different numerical schemes helps shed light on the potential dynamical cause by gauging the sensitivity of the results from the numerical aspect. For such an alternative numerical option, a continuation (homotopy) process is introduced as previously explored by Lantoine and Russell (2011) as well as Almanza-Soto (2023). The homotopy scheme involves introducing a set of intermediate artificial models between the CR3BP and HFEM, where analogs for the CR3BP POs are constructed within these intermediate models. These solutions serve as evolving initial guesses

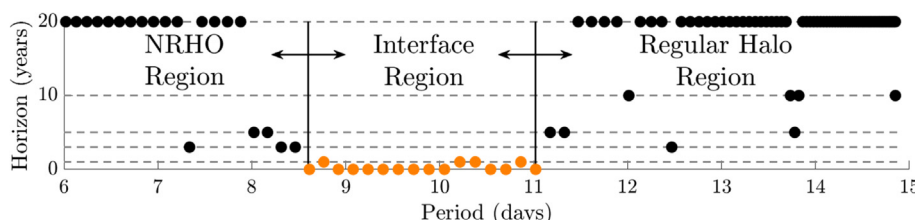


Fig. 8. Maximum time for which an HFEM analog to a halo orbit has been detected as a function of the period.

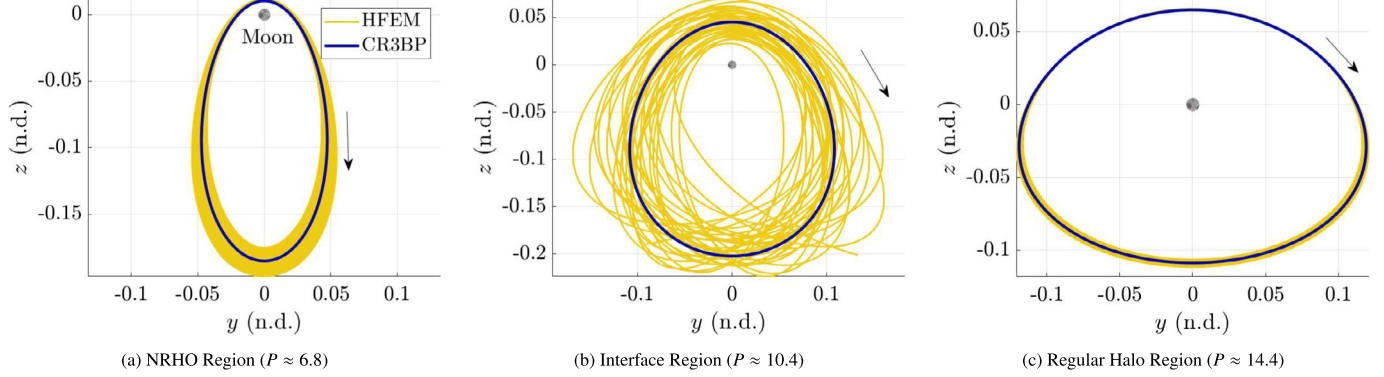


Fig. 9. Sample HFEM result directly transitioned from each region, $\hat{y} - \hat{z}$ projection (pulsating rotating frame), P in days.

for the next intermediate model until the continuation process bridges the gap and reaches the desired HFEM dynamics. This continuation approach effectively breaks down the direct transition problem into a series of smaller and more manageable steps, allowing for a more reliable and smoother transition of HFEM analogs in the Interface Region that overcome the transition-challenging behavior. Thus, if the numerical continuation scheme *fails* to produce the desired transitioned results at an intermediate step, the problem is potentially linked to the perturbations as introduced in the corresponding intermediate model, yielding dynamical insights. In the continuation process, the intermediate models are constructed by interpolating the location of the Earth and the gravitational parameter for the Sun. A continuation parameter ϵ is defined between 0 and 1, and the Earth's position vector is constructed as,

$$\vec{R}_{ME,\epsilon} = (1 - \epsilon)\vec{R}_{ME,C} + \epsilon\vec{R}_{ME}, \quad (14)$$

where $\vec{R}_{ME,C}$ denotes the location of the Earth with respect to the Moon as governed by the CR3BP dynamics, within the inertial frame, and \vec{R}_{ME} refers to the location retrieved from ephemerides. The interpolated position vector $\vec{R}_{ME,\epsilon}$ corresponds to the Earth position within the intermediate model constructed at a specific value of ϵ . Similarly, the solar gravity is evolved via,

$$\tilde{\mu}_{S,\gamma} = \gamma\tilde{\mu}_S, \quad (15)$$

where $\gamma \in [0, 1]$, similar to ϵ . Then, $\vec{R}_{ME,\epsilon}$ and $\tilde{\mu}_{S,\gamma}$ are utilized in place of \vec{R}_{ME} and $\tilde{\mu}_S$ in Eq. (6) for the intermediate models for specified ϵ and γ values. While it is possible to leverage different values for ϵ and γ or even to evolve them in different step sizes, in the current work, $\epsilon = \gamma$ is

employed. Under this formulation, $\epsilon = 0$ denotes the CR3BP dynamics; in this case, the initial guess from the CR3BP POs serves as a trivial solution. Then, incremental steps are introduced in ϵ until $\epsilon = 1$, corresponding to the realistic Sun-Earth-Moon HFEM dynamics. In the current analysis, fifty linearly spaced incremental steps are used to complete this transition from the CR3BP to HFEM. This process is denoted as “direct” continuation to distinguish from continuing within the ER3BP.

Through this direct continuation process, constructing two years of HFEM counterparts are attempted for the Interface Region, and the results are illustrated in Fig. 10. As a two-year interval is generally considered short to fully capture the quasi-periodic structures within the QPOs, the solutions are potentially sensitive to the specifics of the transition process. Therefore, multiple reference epochs are simultaneously examined, placed in two-year steps, corresponding to different colors in the plot. For example, “2021” and “2023” refer to the results with $JD_{fix} = 09/23/2021$ and $JD_{fix} = 09/23/2023$, respectively. The markers in the figure correspond to the maximum ϵ value that the continuation process is able to reach before the targeting process from Eq. (13) fails. Interestingly, across different baseline epochs, the continuation procedure tends to converge to a similar boundary, implying that the failing ϵ values are consistent across multiple epochs. There are a few exceptional cases where the continuation process reaches $\epsilon = 1$, indicating successful transition to the HFEM dynamics. Two sample results corresponding to the “2023” baseline epoch are displayed in Fig. 11. The cases that converge for $9 < P < 9.5$ days typically result in three distinct lobes, as demonstrated in Fig. 11(a). This geometry corresponds to a 3 : 1 sidereal resonance halo

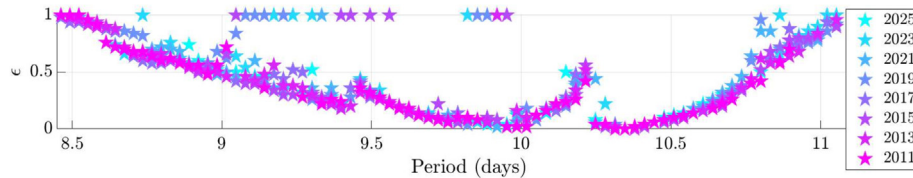


Fig. 10. Maximum continuation parameter, ϵ , from the direct continuation results over two years for a horizon time, Interface Region.

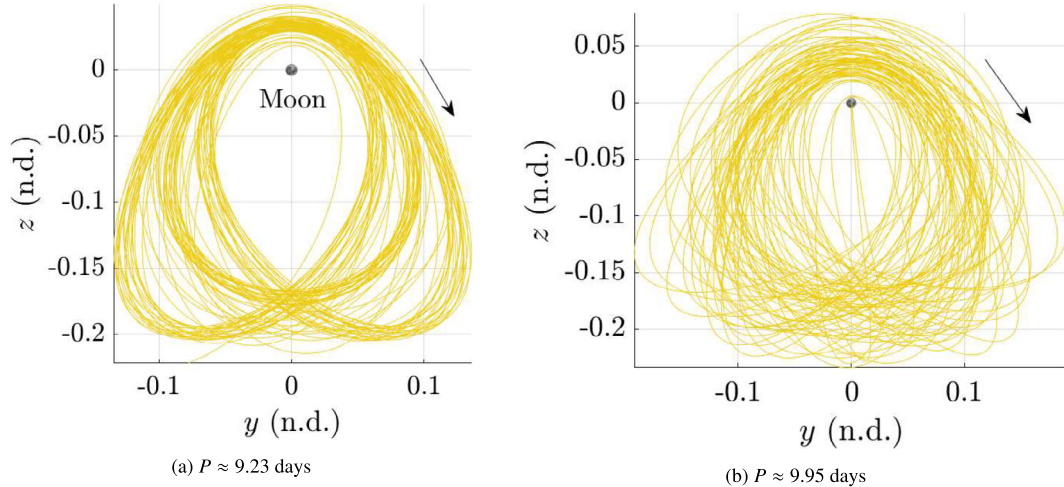


Fig. 11. Sample solutions over two years obtained via the continuation scheme ($JD_{\text{fix}} = 09/23/2023$).

orbit within the ER3BP, as previously noted by [Park and Howell \(2024\)](#). In contrast, the cases near $P = 10$ days are typically associated with more complex geometries, as displayed in [Fig. 11\(b\)](#). While the continuation process produces two years of HFEM counterparts for a few cases, these solutions are not necessarily representative of the behavior of longer HFEM analogs, i.e., the two-year solutions are not likely to be repeatable. The three distinct lobe geometry eventually breaks down for longer horizons when $P \neq 9.1$ days, corresponding to an approximate 3 : 1 side-real resonance ratio. Similarly, the geometries associated with close lunar flybys, as apparent in [Fig. 11\(b\)](#), likely indicate that the geometry is not repeatable over a longer horizon.

To confirm the observation that the results reaching $\epsilon = 1$ in [Fig. 10](#) are not repeatable over longer horizon times, further experiments are conducted with $JD_{\text{fix}} = 09/23/2023$. The results for two, three, and four years for the horizon time are illustrated in [Fig. 12](#). It is noteworthy that while two year-solutions at $\epsilon = 1$ are located for a few cases, utilizing the same reference epoch, the continuation process fails to produce acceptable analogs within the HFEM for the longer horizon times. In summary, the continuation process reveals a boundary for ϵ values at which the given targeting process fails to converge. Although different numerical procedures targeting this specific scenario may yield more favorable outcomes, the current numerical results indicate that the Interface Region is associated with

complex dynamical counterpart behaviors, and longer-term HFEM analogs are challenging to produce. To gain more insights into the dynamical issues for the observed numerical behavior within the given transition approach, such as the breakdown of quasi-periodic structures within the HFEM, further investigation is warranted. Specifically, the boundary behaviors observed in [Figs. 10 and 12](#) suggest that the desired dynamical structures are challenging to locate.. The subsequent sections employ the ER3BP to uncover the underlying dynamical mechanism. In particular, Section 6.2.4 demonstrates that the destruction of these structures at sufficiently large perturbations, e.g., ϵ , from the CR3BP, potentially occurs within the Interface Region.

5. Nominal behavior: ER3BP L₂ Halo counterparts in comparison with the HFEM Analogs

Understanding the behavior of HFEM counterparts is challenging due to their sensitivity in response to the specifics of the numerical transition process. This challenge leads to the exploration of periodically perturbed Hamiltonian systems that incorporates additional forces into the CR3BP in ideal forms. Specifically, the focus shifts to models that predict the numerical behavior of the HFEM analogs, as illustrated in [Figs. 8 and 10](#).

[Park and Howell \(2024\)](#) provide an analytical foundation for selecting a suitable one-frequency Hamiltonian system within the context of transitioning CR3BP struc-

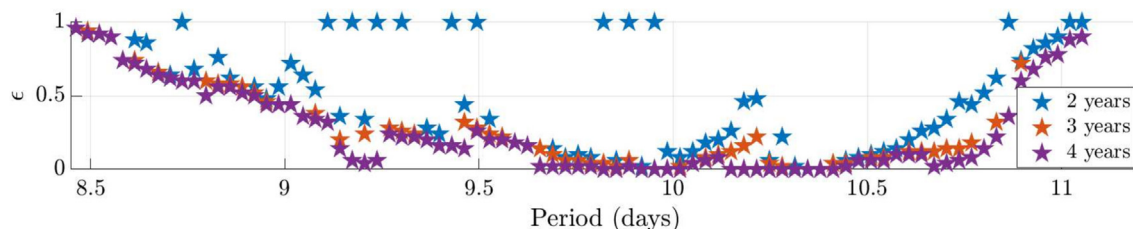


Fig. 12. Maximum continuation parameter, ϵ , from the direct continuation results for two, three, and four years, Interface Region ($JD_{\text{fix}} = 09/23/2023$).

tures into the HFEM. They propose that, for CR3BP orbits associated with small \dot{y} excursions, such as the L_2 halo orbits, the realistic pulsation of the Earth-Moon distance is likely to dominate the geometry change from the CR3BP POs to HFEM analogs. Consequently, the ER3BP stands out as the most desirable one-frequency model among frequently used alternatives, as it approximates the realistic pulsation with both a proper magnitude and a frequency. In this analysis, the global behavior of the HFEM and ER3BP counterparts across the L_2 halo family is compared to assess the HFEM long-term analogs in the vicinity of the ER3BP QPOs. This analysis is first explored for the cases where the **nominal behavior** for the HFEM transition is observed.

5.1. ER3BP QPO continuation results

The ER3BP QPO construction in this analysis is introduced in Section 3.3 along with the ER3BP continuation scheme in B. The global trend across the entire L_2 halo family is summarized in Fig. 13. The horizontal axis denotes the CR3BP period, P , in days. The vertical axis denotes the eccentricity, e , the parameter employed for the QPO continuation process. The process demonstrates two representative behaviors. For most members of the family, notably in the NRHO and Regular Halo Regions, the ER3BP QPOs are successfully continued until reaching the desired eccentricity, $e_d = 0.055$. Recall that this value belongs to a desired range of eccentricity to properly represent the realistic motion of the Earth-Moon system in the HFEM, as discussed in Park and Howell (2024). Then, in the second representative case in the Interface Region, a numerical failure in continuation occurs before reaching e_d . These cases involve a QPO targeting algorithm that fails to converge below a desired tolerance level prior to reaching the maximum number of iterations in the corrections process. The QPO computational algorithm (GMOS, Gómez and Mondelo (2001); Olikara and Scheeres (2012)) approximates invariant curves utilizing a truncated Fourier series, where the accuracy of the approximation depends on the number of parameters employed to construct the series, i.e., N . While $N = 51$ is generally sufficient to represent the curves accurately, it is inadequate when the shape of the invariant curve becomes “complex” due to any local dynamics. In such cases, the GMOS algorithm strug-

gles to locate the invariant curve that satisfies the invariance condition (Eq. (B.5) in B) within the specified tolerance. While it is possible to change the number N , a limit exists due to the computational costs that scale rapidly with N . It is noted that incorporating a larger value for N aids in constructing the QPOs to a slightly higher eccentricity value, but does not lead to the successful continuation until reaching the desirable e_d for multiple test cases.

The continuation diagram in Fig. 13 indeed demonstrates a behavior similar to results for HFEM-analogs constructed and illustrated in Fig. 8. Recall that Fig. 8 is generated with a *direct transition* process that leverages the CR3BP POs as the initial guess in the numerical targeter and shifts directly to the HFEM. Thus, the construction of QPOs faces significant challenges also within the Interface Region. Note that some continuation challenges also exist outside of the Interface Region. These challenges are typically associated with resonance gaps (Olikara et al., 2016), where the corresponding resonance ratios are included in Fig. 13. In the vicinity of the p:q resonance ratio, the QPOs approach the shape of the resonant POs, also observed by Rosales et al. (2021) within the Bi-Circular Restricted Four-Body Problem (BCR4BP). Near each strong resonance ratio, often associated with small integers for p and q , larger N values are required to suitably represent the invariant curves, clarifying some of the numerical difficulties in NRHO Region and Regular Halo Region as illustrated in Fig. 13.

5.2. HFEM and ER3BP comparison - hyperplane examination

Based on Figs. 8 and 13, it is evident that both the 20-year HFEM solutions and ER3BP QPOs are relatively well-defined within the NRHO and Regular Halo Regions. Recall that the regions reflect the **nominal behavior** from the previous section. Given this observation, the similarities between the counterparts from the HFEM and ER3BP are investigated in these regions to demonstrate that the HFEM 20-year analogs indeed form in the vicinity of the ER3BP QPOs. For this analysis, 12 different HFEM counterparts are selected from Fig. 14(a), spanning a 20-year range. These orbits are highlighted in yellow within the figure. The corresponding geometries within the rotating

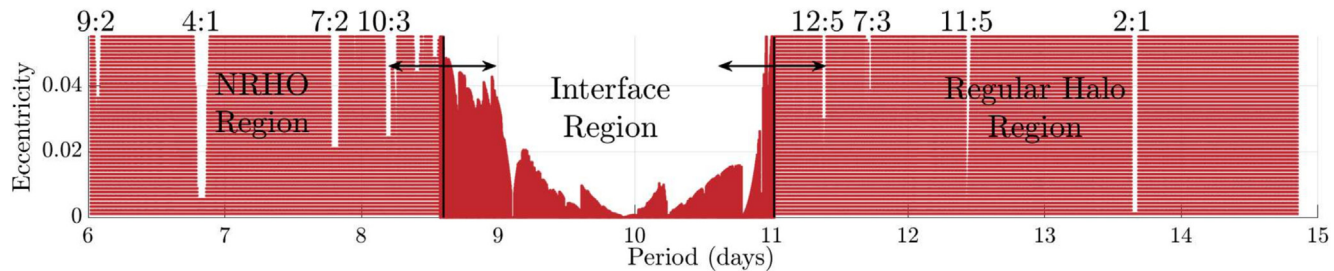


Fig. 13. Maximum eccentricity values from the ER3BP QPO continuation results - the boundaries from Fig. 8 are overlaid.

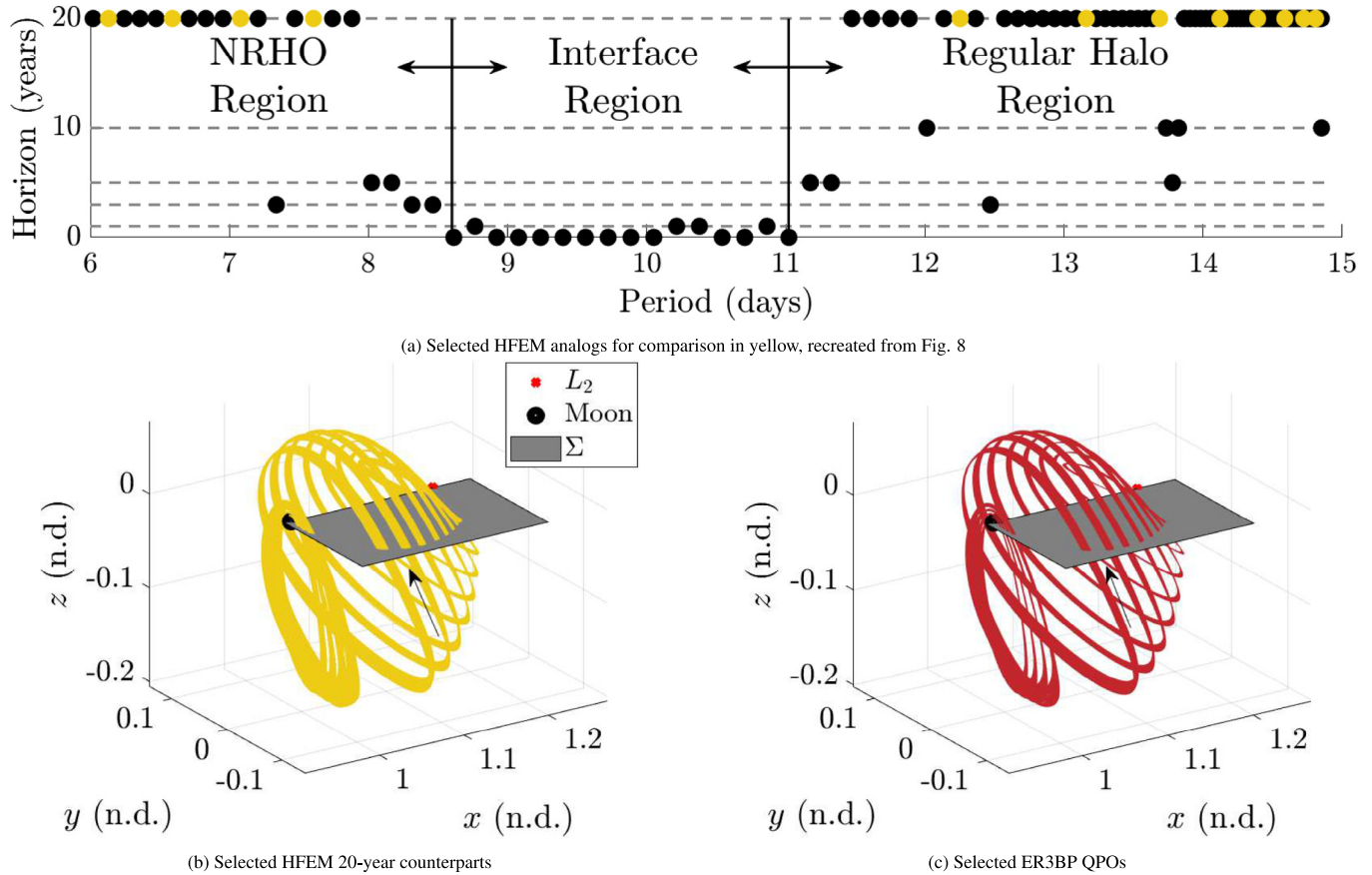


Fig. 14. HFEM and ER3BP counterparts for the 12 specific orbits.

frame are visualized in Fig. 14(b). In the pulsating-rotating frame, a hyperplane is constructed at $z = 0$ ($\dot{z} > 0$) and represented by the gray surface in the figure. Additionally, Fig. 14(c) displays the ER3BP QPOs emanating from the same respective P (period) along with the hyperplane.

The position crossings on the hyperplane from both the HFEM solutions and the ER3BP QPOs are recorded and visualized in Fig. 15. Within the figures, the blue star corresponds to the crossing from the respective CR3BP PO with the same P . The comparison, not surprisingly, indicates that the HFEM crossings in yellow exhibit more complex behavior as compared with the ER3BP counterparts in red. However, despite this difference, a noticeable similarity between the HFEM and ER3BP crossings within the NRHO and Regular Halo Regions is evident. Throughout these regions, similar behavior is observed, not just limited to the 12 selected orbits in this analysis. Thus, it is visually demonstrated that the multi-year HFEM solutions are formulated in the vicinity of the ER3BP QPOs in general within the L_2 halo family.

Other observations are also apparent in Fig. 15. Offsets in the position crossings are sometimes apparent, such as in Fig. 15(j), where the HFEM crossings result in slightly higher y values as compared to the ER3BP counterparts. This offset is due to the lack of a phase constraint within the HFEM transition process. In contrast to the ER3BP

QPO continuation process that fixes the underlying P or ρ_E within the f -domain, the current HFEM targeting process does not explicitly constrain either. Rather, the targeting process locates a nearby solution that exists in the vicinity of the stacked CR3BP POs with the given initial guess scheme represented in Eqs. (7)–(10). Fig. 15(l) displays a HFEM trajectory that deviates further from the ER3BP crossings. This specific case corresponds to halo orbits in the vicinity of the bifurcating Lyapunov orbit, where multiple nearby structures exist, including northern halos, Lyapunov orbits, and Lissajous orbits (Lian et al., 2013). Thus, it is possible that the current numerical scheme converges to one of the analogs more closely associated with these nearby structures' analogs rather than converging to the desired L_2 halo orbit counterpart.

5.3. HFEM and ER3BP comparison - Fourier analysis

The visual similarities observed in the hyperplane crossings in Fig. 15 are further supported by frequency analysis. This analysis indicates that the HFEM and the ER3BP counterparts not only share similarities in their positions within the hyperplane but also exhibit *common frequency structures*. To conduct the Fourier analysis, multiple state samples along the analogs are collected across evenly spaced independent variables, serving as the input signal

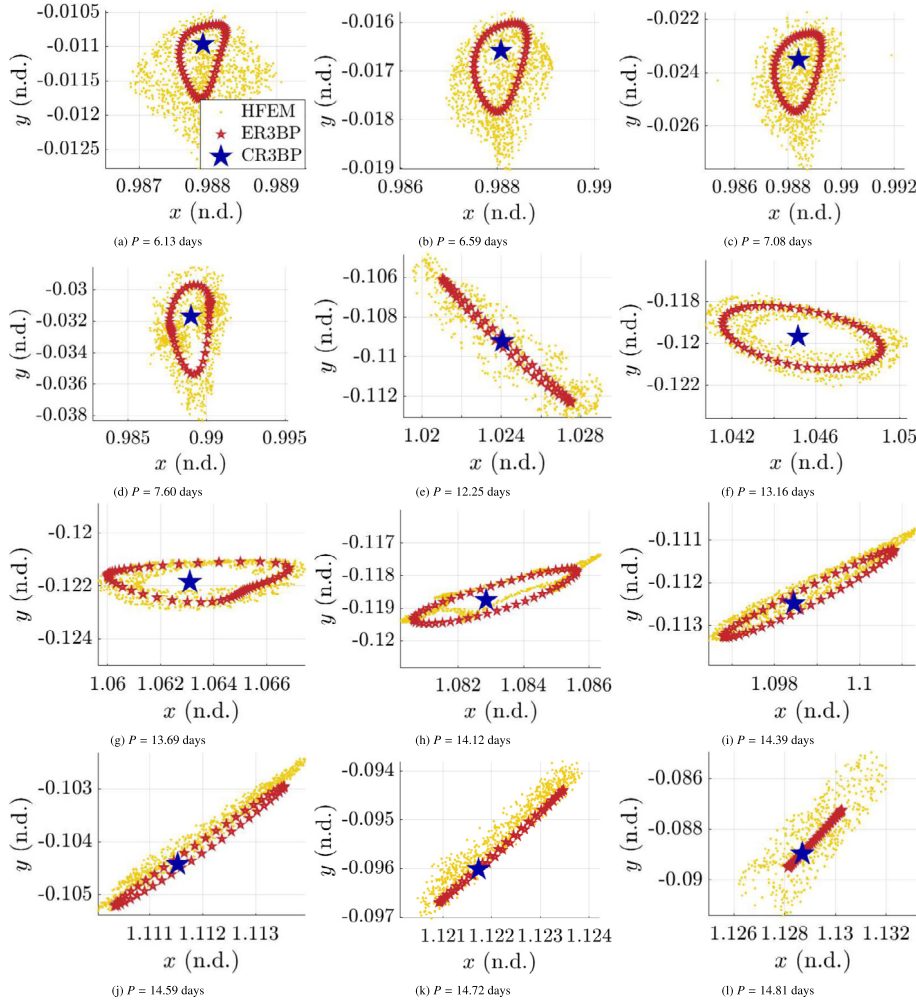


Fig. 15. HFEM and ER3BP Earth-Moon L₂ halo counterparts comparison - hyperplane examination.

for the Discrete Fourier Transform (DFT). The DFT then provides spectral domain information for the respective counterparts. Ideally, consistent with Gómez et al. (2002), assuming that the multi-year HFEM analogs indeed leverage quasi-periodic structures, it is expected that the DFT analysis on the HFEM solutions reveals frequency structures that are represented as linear combinations of v_p (the underlying CR3BP PO frequency) and the fundamental frequencies from the HFEM itself (Jorba and Villanueva, 1997). However, there are certain considerations and potential challenges in this DFT approach. Firstly, familiar issues are encountered with DFT, such as spectral leakage, finite frequency resolution, and aliasing (Lyons, 1997), that complicate the accurate detection of frequencies associated with the signal. Additionally, the constructed HFEM analogs are only continuous up to the desired tolerance and are technically not Hamiltonian structures, implying that the frequency structures potentially include some frequencies that are not explicitly modeled as the HFEM fundamental frequencies. Consequently, the frequencies observed through the DFT may not be represented with a finite set of fundamental frequencies that suggests caution in interpretation of the results.

Another relevant issue in the current analysis is that the dynamical models being investigated evolve with distinct independent variables. Comparing the frequency domain information requires defining a consistent independent variable to establish a common basis for comparison. To this end, the nondimensional time variable t from the CR3BP is adopted as the common independent variable. However, determining the *isochronous correspondence* between dimensional time T (HFEM) and nondimensional time t (CR3BP), and true anomaly f (ER3BP) together poses challenges as these functions are generally arbitrarily defined, potentially changing the information apparent in the frequency domain with respect to t . In this analysis, insights from Park and Howell (2024) are leveraged to construct suitable functions. Note that a core property of the characteristic time within the CR3BP utilizes $t_* = \sqrt{l^3}/(\tilde{\mu}_E + \tilde{\mu}_M)$. Thus, the independent variable from the HFEM, T , is assumed to be correlated with t via the relationship,

$$\frac{dt}{dT} = \sqrt{\frac{\tilde{\mu}_E + \tilde{\mu}_M}{R_{EM}^3(T)}}, \quad (16)$$

where the instantaneous distance between the Earth and the Moon is leveraged to construct the instantaneous characteristic time that preserves the CR3BP property. Note that the same relationship is incorporated for constructing patchpoints in the direct transition process as accomplished in Eq. (10). Similarly, the independent variable for the ER3BP, f , and t , are related via the dependency,

$$\frac{dt}{df} = \frac{1}{\sqrt{1 + e \cos f}}, \quad (17)$$

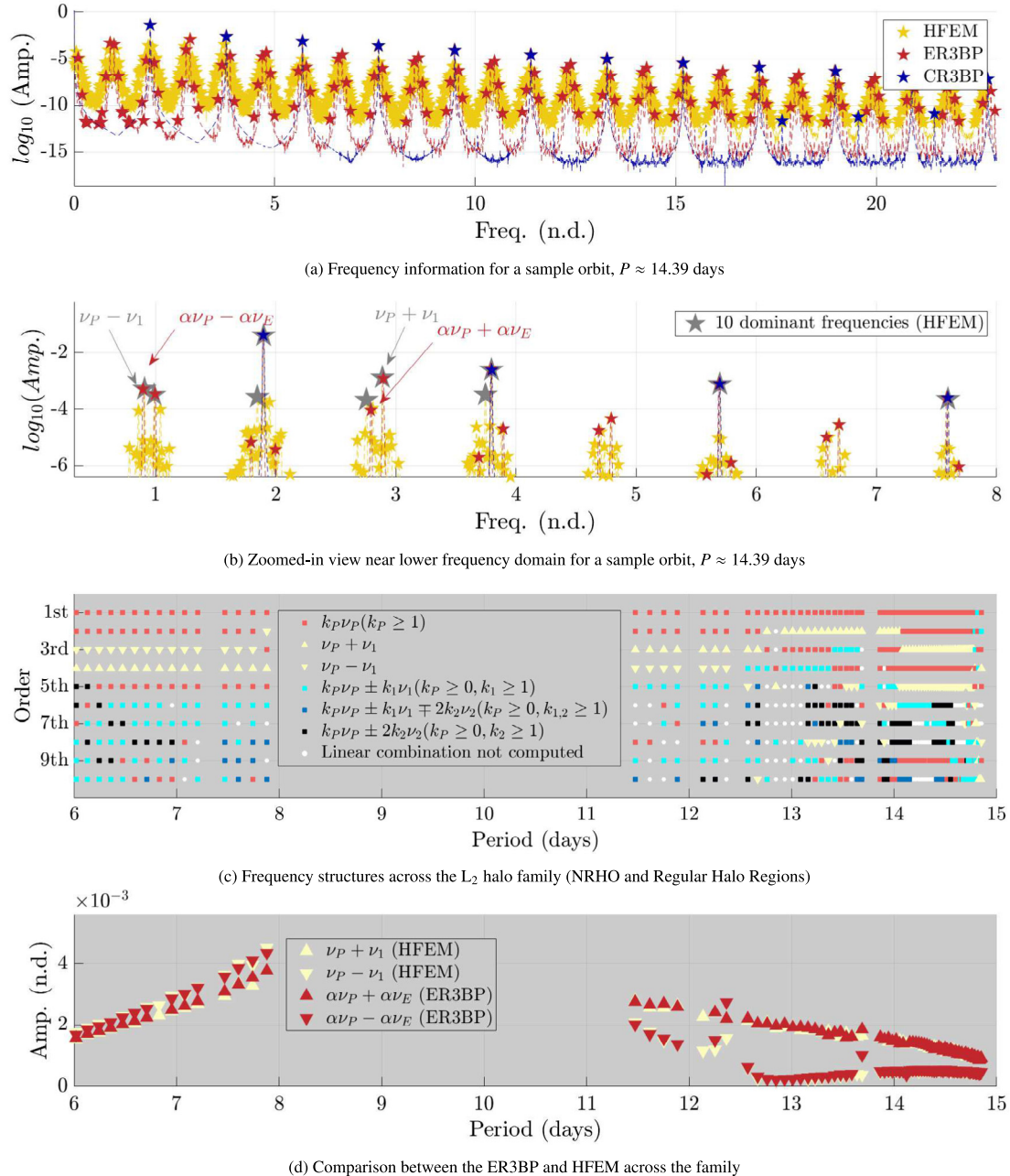
where a conic equation is employed for the derivation that also preserves the CR3BP nondimensionalization properties. For further interpretation of these isochronous correspondence functions and derivations, refer to Park and Howell (2024). Then, 2^{14} samples are collected from 20 years of CR3BP POs, ER3BP QPOs, and HFEM solutions that are evenly placed in t utilizing Eqs. (16) and (17). While all 6-dimensional state components illustrate similar behavior, the \hat{x} position component is investigated in the current work as an example. Note that the minimum resolution of the detected frequency is solely a function of the solution horizon time that scales with $2\pi/\Delta t$ (Lyons, 1997), where Δt is the total horizon time as the nondimensional unit. While it is desired to investigate a long horizon time for a higher resolution of the frequency in general, it is currently capped at 20 years. Also, it is advised to leverage a “sufficiently-high” sampling rate to minimize aliasing within the higher frequency domain. The current selection for number of samples (2^{14}) is sufficient as the subsequent analysis focuses more on the lower frequency domain. Finally, the signal, e.g., the \hat{x} position values over the 2^{14} samples, is multiplied by a Hanning window function of order 2 to alleviate the spectral leakage; this approach is consistent with previous investigations (Gómez et al., 2010; Dei Tos and Topputto, 2017). Note that, while different numerical formulations for the DFT may alter the specific results, the current approach proves sufficient to illustrate the similarity between the HFEM and the ER3BP frequency responses.

Within the common t -domain, three *core* frequencies are expected to emerge for the HFEM analogs. The first type of frequency is $v_p = 2\pi/P$, associated with the period P of the underlying CR3BP POs. While no phase constraints are introduced in the HFEM transition process, the times corresponding to the patchpoints, T_i , are constructed using Eq. (10); the average “period” for the HFEM substitutes within the t -domain is expected to occur near the original P from the CR3BP PO that is employed for the initial guess. Then, two fundamental frequencies associated with the HFEM are examined: $v_1 \approx 0.9896$ and $v_2 \approx 0.9234$, in the t -domain, mainly associated with the pulsation of the Earth-Moon distance and the solar position within the $\hat{x} - \hat{y}$ plane, respectively. For more accurate physical interpretations of these frequencies, refer to Gómez et al. (2002) as well as Park and Howell (2024). While previous authors note the existence of three additional frequencies, the

contributions from these frequencies are typically associated with lower amplitudes compared to the influence from v_1 and v_2 , and are not considered in the current work. In short, the frequencies from the HFEM counterpart are investigated in terms of the linear as well as the integer combinations of v_p, v_1 , and v_2 .

Similarly, from the DFT on the ER3BP QPOs, two *core* frequencies are expected. While within the f -domain, these frequencies are fixed as $v_p = 2\pi/P$ and $v_E = 1$ (corresponding to the ER3BP’s model frequency), transforming the independent variable from f to t results in slightly different frequencies. Specifically, in the t -domain, the ER3BP QPO that originates from the CR3BP PO with v_p is associated with αv_p and $\alpha v_E = \alpha$, where $\alpha \approx 0.9994$ with $e = 0.055$. This value is numerically determined since Eq. (17) is an elliptic integral that does not yield a closed-form solution. Note that $\alpha v_E \neq v_1$ is associated with the fact that the pulsation in the HFEM includes the precession of the lunar perigee due to the solar gravity that the ER3BP lacks. This discrepancy implies that the frequency “error” from the ER3BP gradually builds up over a long-horizon solution and adjustments are required when the ER3BP structures are leveraged as initial guess to deliver the HFEM analogs (Park and Howell, 2024). For an ER3BP QPO that emanates from a CR3BP PO with v_p , the frequency spectrum is expressed as the linear as well as the integer combinations of αv_p and αv_E .

Consider the frequency domain information illustrated in Fig. 16(a), generated for $P \approx 14.39$ days. The horizontal axis of the plot denotes the nondimensional frequency with respect to t . The vertical axis corresponds to the \log_{10} of the respective amplitude (Amp.). The stars denote the peaks in DFT spectra, colored differently to correspond to the CR3BP PO, the ER3BP QPO, and the HFEM 20-year analogs. Note that the peaks associated with the CR3BP trajectory correspond to $k_p v_p$, where k_p is a positive integer. The shape of the halo orbits in the rotating frame allows a progressive attenuation (or decay) in amplitude relative to the frequency. Note that, in the vicinity of the CR3BP peaks, the ER3BP and HFEM trajectories also produce peaks with similar magnitudes. Thus, the HFEM and ER3BP spectra are associated with peaks at $k_p v_p$ and $\alpha k_p v_p$, respectively. This behavior is expected, since the counterparts, in general, remain in the vicinity of the original CR3BP halo orbits as constructed within the rotating frame. While the HFEM spectrum demonstrates more complex behavior in general, focusing on the first few dominant frequencies in the lower-frequency domain provides valuable insights. Fig. 16(b) offers a zoomed-in view of the lower-frequency domain for the same orbit, where the gray stars are added and represent the frequencies associated with the first 10 dominant amplitudes for the HFEM results. In general, these frequencies are expected to be approximated as linear combinations of v_p, v_1 , and v_2 , i.e., $v \approx k_p v_p + k_1 v_1 + k_2 v_2$, where k denotes the integer coefficient for each core frequency. Due to the limited accu-

Fig. 16. HFEM and ER3BP Earth-Moon L₂ halo counterparts comparison - Fourier.

racy of the spectral analysis, it may be challenging to locate a specific combination of k_p, k_1, k_2 that results in an exact representation. The problem is further compounded whenever v_1 or v_2 are in near-resonance with v_p ; in such cases, multiple combinations exist that approximate a given value of v . To alleviate this issue, an algorithm is introduced that leverages the intuition regarding the most dominant frequencies to sequentially locate them. This intuition involves the fact that the frequency domain response displays a “regular” behavior, i.e., the amplitudes generally decrease for higher frequencies as evident from a sample plot in Fig. 16(a). Thus, it is expected that the first few dominant frequencies are associated with a small number

for $|k_p| + |k_1| + |k_2|$, where ≤ 6 is used in the current work. Then, several groups of patterns for combinations are identified as: $\vec{v}_{\text{group},1} = [k_p v_p \mid 1 \leq k_p \leq 6] = [v_p, 2v_p, \dots, 6v_p]^T$; $\vec{v}_{\text{group},2} = [k_p v_p + k_1 v_1 \mid |k_p| + |k_1| \leq 6, |k_1| \geq 1]$; $\vec{v}_{\text{group},3} = [k_p v_p + k_1 v_1 + k_2 v_2 \mid |k_p| + |k_1| + |k_2| \leq 6, |k_2| \geq 1]$. These groups of frequencies are derived from an empirical perspective via investigating multiple frequency responses for several examples. The first group locates multiples of the underlying CR3BP PO frequency, v_p . While the HFEM dynamics perturb the CR3BP geometry, it is expected that these frequencies survive as the HFEM solutions inherit the motion in the CR3BP as illustrated in Fig. 9(a) and (c). Then, the second group consists of v_p and v_1 , observing

that the HFEM solutions are in close proximity to the ER3BP QPOs in Fig. 15 and noting the analytical prediction from Park and Howell (2024). The last group is comprised of all three frequencies of interest, v_P , v_1 , and v_2 . Then, for each set of potential candidates for the group of frequencies, Algorithm 1 is leveraged to locate the linear combinations k_P, k_1, k_2 for the first 10 dominant peaks and the corresponding frequencies, i.e., v_{i-th} for $1 \leq i \leq 10$. Specifically, for each group, possible combinations for k_P, k_1, k_2 are recorded that result in the smallest error, err_{min} . Then, for each combination, if the error is below the tolerance level, for this analysis equal to $0.01v_P$, such a combination of integers, \vec{k}_{i-th} , is assigned for the i -th dominant frequency, v_{i-th} . If such a combination is not identified, the next group of frequencies is investigated. The process is repeated until the combinations for the 1st through 10th frequencies are located. A sample result is illustrated in Table 2 that corresponds to Fig. 16(b). The frequencies are ordered by the amplitude for each column. The last row corresponds to the difference between the detected frequency and the linear approximation, denoted as $\Delta v = v - (k_P v_P + k_1 v_1 + k_2 v_2)$. In this example, Algorithm 1 is successful in identifying the combinations of v_P, k_1, k_2 that accurately explain the constructed frequency domain response.

Algorithm 1. Frequency detection algorithm

Algorithm 1 Frequency detection algorithm

Input: the first 10 dominant peaks v_{i-th} with $1 \leq i \leq 10$
Output: the linear coefficient vectors $\vec{k}_{i-th} = [k_P, k_1, k_2]^T$
 $v_C \leftarrow$ initialized from the CR3BP PO

```

for  $i = 1$  to  $10$  do
     $j, err_{min}, v_{min} \leftarrow$  reset
    repeat
         $err_{min} \leftarrow \min_{v \in \vec{v}_{group,j}} (v_{i-th} - v)$ 
         $v_{min} \leftarrow \operatorname{argmin}_{v \in \vec{v}_{group,j}} (v_{i-th} - v)$ 
         $j \leftarrow j + 1$ 
    until  $err < tol$  or  $j > 3$ 
     $\vec{k}_{i-th} \leftarrow \vec{k}(v_{min})$ 
return  $\vec{k}_{1st}, \dots, \vec{k}_{10th}$ 

```

▷ min returns the minimum err
▷ $argmin$ returns $v \in \vec{v}_{group,j}$ that minimizes err
▷ A zero vector is assigned for $j > 3$, corresponding to failure

Two observations are noteworthy from the sample output in Fig. 16b) and and Table 2. First, $v_P \pm v_1$ emerge as the most dominant perturbations that cannot be expressed as multiples of v_P . Frequencies other than $k_P v_P$ are indeed associated with the quasi-periodic nature of the HFEM counterparts, where the perturbations most often originate from v_1 and v_2 . As evident from the decaying behavior of the spectrum in Fig. 16(a), the relative magnitude of the lower frequencies effectively represents the order of perturbations as well. In this specific example, the perturbation originating from $v_P + 2v_2$ is only 25% as compared to the

perturbation from $v_P + v_1$ ¹. Secondly, note that the ER3BP QPO also exhibits similar amplitude levels for the same structure of frequencies, i.e., $\alpha v_P \pm \alpha v_E$, as apparent in Fig. 16(b). This observation suggests that the ER3BP QPOs share common frequency traits with the HFEM counterparts. The investigation extends across the entire L₂ halo family to explore the trend regarding these two behaviors.

The dominant impact from $v_P \pm v_1$ is established by examining the frequency structures associated with the first 10 dominant amplitudes across the entire family utilizing Algorithm 1. Fig. 16(c) illustrates the frequency structure for the 20-year HFEM analogs. The horizontal axis corresponds to the period P of the underlying CR3BP PO, while the vertical axis denotes the order of the amplitudes corresponding to the peaks produced from the DFT. It lists the first 10 dominant peaks, i.e., 1st, 2nd, ...10th. Different markers denote different structures for the respective frequencies, where the detected frequencies are approximated as linear combinations of v_P, v_1 , and v_2 utilizing Algorithm 1. In Fig. 16(c), the blank spaces reflect P values where 20-year HFEM solutions are not retrieved (Fig. 8), or where the detected frequency is not represented as a linear combination of v_P, v_1 , and v_2 to within a given tolerance, set to be $0.01v_P$. These occurrences most often arise due to the inherent limitations of the DFT in accurately detecting frequent-

cies, as previously discussed, or, cases where the rest of the fundamental frequencies, besides v_1 and v_2 , within the HFEM are required. However, the patterns disclosed in

¹ While the perturbations that involve v_2 are generally smaller ($\approx 25\%$) as compared to those from v_1 , it may be desired to model such perturbations during a preliminary analysis. While the ER3BP alone faces challenges in modeling the v_2 -related components, intermediate models that simultaneously include v_1 and v_2 may be introduced to further bridge the gap between the CR3BP and HFEM. For an example for such a quasi-periodically forced dynamical model, refer to Park et al. (2024).

Table 2

First 10 dominant frequencies (gray stars from Fig. 16(b))

Order	1st	2nd	3rd	4th	5th	6th	7th	8th	9th	10th
Freq. (n.d.)	1.8994	3.7961	2.8880	5.6955	0.9081	3.7461	0.9886	1.8467	7.5949	2.7547
$\log_{10}(\text{Amp.})$ (n.d.)	-1.3940	-2.6131	-2.8859	-3.1215	-3.2858	-3.4913	-3.4993	-3.5745	-3.6499	-3.6751
k_P	1	2	1	3	1	1	0	0	4	1
k_1	0	0	1	0	-1	0	1	0	0	-1
k_2	0	0	0	0	0	2	0	2	0	2
Δv (n.d.)	0.0010	0.0008	0.0000	0.0002	0.0008	0.0009	0.0010	0.0001	0.0012	0.0009

Fig. 16(c) are deemed sufficient to illustrate the general behavior. The most dominant frequencies typically appear as $k_P v_P$ (■), corresponding to multiples of the underlying CR3BP PO frequency, where k_P is a positive integer. It is expected that the first dominant frequency is always $k_P v_P$ with $k_P = 1$, with an exception occurring near $P = 14.8$ days. This exception corresponds to the region near the bifurcating Lyapunov orbit, where the targeter may leverage various nearby structures, as also apparent from Fig. 15(l). Similarly, the second dominant frequency is $2k_P$ for most orbits. It is noticed that $v_P \pm v_1$ (▲, ▽) usually exhibit larger amplitudes as compared to other perturbing frequencies. The amplitudes originating from v_2 (■, ▨), considered to be generally associated with the solar gravity, are typically associated with smaller amplitudes across the family.

The amplitudes corresponding to $v_P \pm v_1$ (▲, ▽) and $xv_P \pm xv_E$ (▲, ▽) are also compared between the HFEM and ER3BP spectra. Fig. 16(d) illustrates that the amplitude associated with each frequency structure displays very similar magnitudes across the two models. This observation aligns with the hyperplane examination, where the trajectories constructed in the ER3BP exhibit representative behavior for the HFEM counterparts as well. Due to the inherent discrepancy in the independent variables employed for the HFEM and ER3BP, the HFEM solutions do not exactly leverage the ER3BP QPOs originating from the same CR3BP PO. However, it is sufficient to conclude that, for this orbit family, the HFEM long-term analogs are formulated in the vicinity of the ER3BP QPOs, and the ER3BP structures effectively approximate the quasi-periodic structures within the HFEM. Again, this observation applies for the NRHO and Regular Halo Regions as classified in Figs. 8 and 13, corresponding to a subset of the L₂ halo family where the long-term HFEM analogs and the ER3BP QPOs are well-defined.

The observation that the HFEM long-term counterparts exist in the vicinity of the ER3BP QPO structures holds important implications. First, the results align with the analytical results from Park and Howell (2024), where pulsation, mainly associated with v_1 , emerges as the dominant source of perturbations for the L₂ halo orbits, rather than the solar gravity that is primarily associated with v_2 . The numerical investigation here confirms the validity of the

formulation proposed in Park and Howell (2024). Secondly, while various periodically perturbed Hamiltonian systems exist and offer valuable insights into higher-fidelity models, it is not always clear which behavior is preserved in the numerical processes from these intermediate models into the HFEM. The results produced through both hyperplane and frequency analyses provide a solid and comprehensive approach to justify the conclusion that the HFEM solutions primarily rely on quasi-periodic structures resembling the ER3BP QPOs for this specific dynamical regime in the L₂ halo family.

The specific results in this section depend on the eccentricity value used for the Earth-Moon system, assumed here to be $e_d = 0.055$. This value lies within the range of desired eccentricity values reported in the literature, e.g., $0.05 \leq e \leq 0.055$, from Park and Howell (2024). While the precise results may vary with different eccentricity values, the ER3BP is expected to exhibit qualitatively similar behaviors across the specified eccentricity range, making the analysis presented here generalizable within the range of desired eccentricity values. For instance, although the amplitudes of the peaks in Fig. 16(b) vary as a function of eccentricity, the overall structure remains consistent. Specifically, the secondary peaks are located at $\alpha v_P \pm \alpha v_E$; This frequency structure highlights the strong connection between the ER3BP and the HFEM.

6. Characterizing transition-challenging behavior with the ER3BP

The nominal behavior observed in the HFEM is primarily characterized by the presence of ER3BP QPOs, as illustrated in Fig. 13. This observation leads to the subsequent question on the correlation between the transition-challenging behavior within the HFEM and the solution behavior within the ER3BP structures. A crucial inquiry arises: what underlying dynamical factor complicates the computation of ER3BP counterparts at the realistic eccentricity value of $e_d = 0.055$? This section introduces two distinct bifurcation behaviors within the ER3BP that differentiate between nominal behavior, where CR3BP POs transition smoothly to the HFEM, and challenging cases with the numerical continuation strategies employed here. These behaviors are validated within a global context

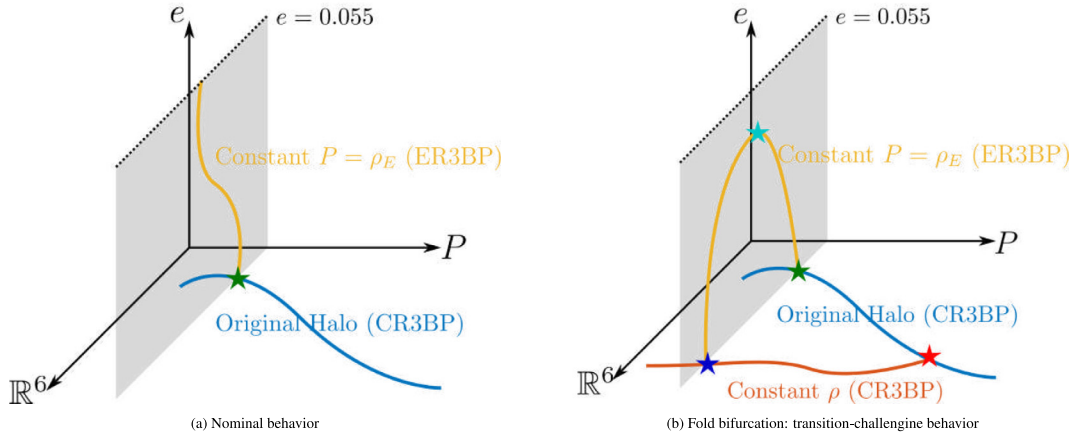


Fig. 17. Two representative bifurcation diagrams.

across the Earth-Moon L₂ halo family. The investigation extends its scope to both ER3BP POs and QPOs, providing a more comprehensive analysis.

Two bifurcation diagrams appear in Fig. 17, illustrating two representative behaviors, namely, the nominal behavior (Fig. 17(a)) and the fold bifurcation (Fig. 17(b)), reflecting the evolution of any CR3BP PO into the corresponding ER3BP structures, either the PO or QPO. Note that the three axes constitute a generic hodograph to depict the evolution of the relevant structures. For the original L₂ halo orbits, constructed within the CR3BP ($e = 0$), the family evolves with the fixed point $\vec{s} \in \mathbb{R}^6$ and the associated period, P . For the fixed point, the reference longitudinal angle of $\theta_{P,0} = 0$ rad is consistently employed. The third axis in the plot corresponds to the eccentricity, e . Following the discussions from Section 3.3, only $e \geq 0$ is employed to represent evolution of the structures. Note that the bifurcation diagrams are applicable to both the ER3BP POs and QPOs.

6.1. Nominal behavior (Fig. 17(a))

For the nominal behavior, the ER3BP structures that emanate from the CR3BP are readily continued to the realistic eccentricity value, $e = 0.055$, without a *turn* in eccentricity (yellow in Fig. 17(a)). The dynamical characteristics of the continuation process in eccentricity are discussed in terms of the possible evolutionary path.

6.1.1. CR3BP → ER3BP bifurcation (★)

The dynamical evolution of the ER3BP structures for the nominal behavior (Fig. 17(a)) is characterized by a single bifurcation, denoted as ★. The ER3BP branch originates from the bifurcation of the original CR3BP family at ★, initiated by the loss of the trivial eigenvalue pair, $\lambda_{1,2} = 1$. The continuation process along the yellow branch assumes a constant stroboscopic mapping time P , as

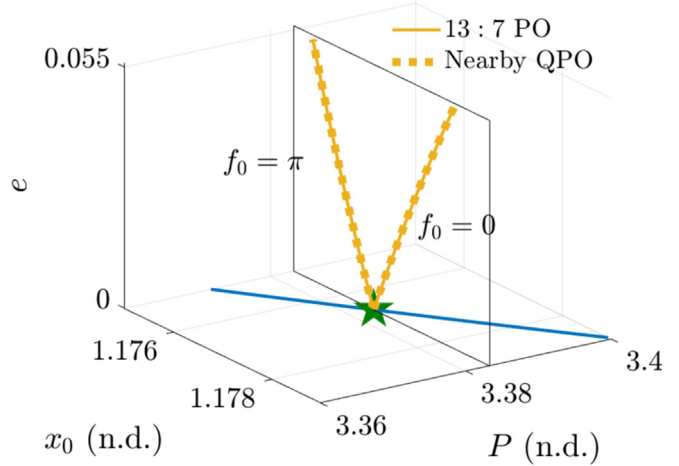


Fig. 18. Nominal case: ER3BP 13 : 7 PO and a nearby QPO bifurcation diagrams.

illustrated by the gray surface in Fig. 17(a). The rotation number ρ_E also remains constant for this branch, governed by the ER3BP dynamics. Subsequently, the nominal case demonstrates a monotonic increase in eccentricity until the continuation process reaches $e_d = 0.055$.

6.1.2. Example - ER3BP 13 : 7 PO and a Nearby QPO

For illustration of the nominal behavior, consider a ER3BP PO that is associated with a resonant ratio, 13 : 7. In this case, the stroboscopic mapping time is fixed as $P = 7 \cdot 2\pi/13 \approx 3.383253$ n.d.. The three-dimensional hodograph is plotted in Fig. 18, where the x -axis of the plot corresponds to x_0 at $\theta_{P,0}$, and the other two axes denote P and e , respectively, consistent with the notation from Fig. 17(a). Note that two counterparts bifurcate from the same point (★) for the POs, corresponding to two separate lines as depicted in Fig. 18. As p is an odd number, $p = 13$, the second counterpart corresponds to an initial true

anomaly of $f_0 = \pi$ rad. Subsequently, a nearby QPO associated with a fixed $P \approx 3.383250$ n.d. is also continued. Since the invariant curve for the QPO spans all f_0 angles between 0 and 2π , $f_0 = 0$ and $f_0 = \pi$ are selected for comparison with the two counterparts for the 13 : 7 POs. Visually, it is evident that the nearby QPO closely approximates the hodographs traced by the two counterparts for the POs. This particular period corresponds to approximately 14.7 days and is far from the predetermined transition-challenging region. Thus, the nominal behavior manifests, wherein both the PO and QPO hodographs continue to $e_d = 0.055$ without a turn in eccentricity.

6.2. Fold bifurcation: transition-challenging behavior (Fig. 17(b))

A more complex scenario commonly occurs in the region where the CR3BP to HFEM transition is particularly challenging, involving the fold bifurcation. A representative case is illustrated in Fig. 17(b), showcasing four distinct types of bifurcations visualized with different colors (\star , \star , \star , \star). As the first type of bifurcation in the family from the CR3BP to the ER3BP (\star) is common in both cases depicted in Fig. 17(a) and (b), explanations are provided for the other three bifurcations.

6.2.1. Fold bifurcation (\star)

In a more general sense, a fold bifurcation is a type of tangent bifurcation where a stability change occurs as an eigenvalue pair from the monodromy matrix M passes through +1 within the complex plane. However, located at an extremum, it does not result in the generation of a new family of solutions. When a new family is generated, transcritical or pitchfork bifurcations occur, facilitating an intersection between the old and the new families. In the current work, a fold bifurcation refers to a *turn* in the eccentricity, or, as demonstrated in Fig. 17(b), a local extremum in eccentricity along the hodograph. As discussed in A, whenever this local extremum behavior is observed, the eigenvalues for the monodromy matrix admit a unity

pair, with the eigenvector coinciding with the local family tangent direction as depicted in the hodograph.

6.2.2. Resonance bifurcation (\star)

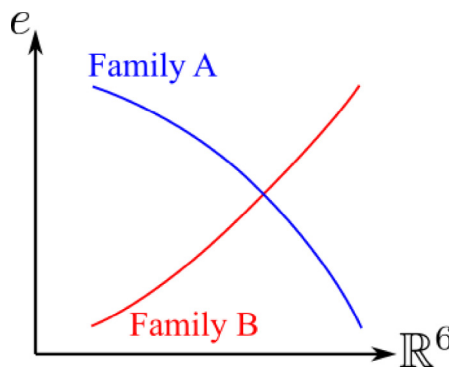
After a turning point (\star), it is possible for the ER3BP family to evolve back to zero eccentricity, connecting to a distinct CR3BP solution that differs from the original bifurcating point, i.e., $\star \neq \star$. This bifurcation is labeled a "resonance bifurcation" because the rotation numbers emerging from both the ER3BP and CR3BP dynamics are in resonance at this bifurcation point, i.e., $\rho = \rho_E + 2k\pi$ for an integer k . Through this process, a new family within the CR3BP is exposed, highlighted in red in Fig. 17(b). It is possible to continue this family within the $e = 0$ plane, now allowing P to change, corresponding to the CR3BP PO or QPO branch with a fixed rotation number, ρ .

6.2.3. Period-multiplying (PO)/ Hopf (QPO) bifurcation (\star)

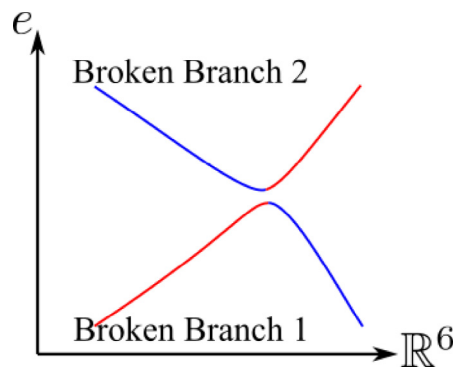
It is possible that the constant ρ branch within the CR3BP continues back to the original halo orbit family, connected via a bifurcation at \star . For the periodic orbits, this bifurcation corresponds to a period-multiplying bifurcation where ρ is in resonance with 2π . In contrast, when ρ is not in resonance with 2π , the bifurcation is denoted as Hopf, secondary Hopf, or Naimark-Sacker bifurcations (Seydel, 2009).

6.2.4. Relationship to broken bifurcations and significance within the context of HFEM transition

Perfect transcritical or pitchfork bifurcations allow an intersection between two continuous families that share a common member at the intersection point. The term "broken bifurcations" denotes cases where these perfect intersections, typically under a perturbation parameter (Seydel, 2009), are destroyed, resulting in two continuous branches that are disconnected. This behavior is commonly reported in various four-body restricted body problems by multiple investigators (Olikara et al., 2016; Henry et al.,



(a) Perfect bifurcation: true intersection



(b) Broken bifurcation

Fig. 19. Perfect and Broken bifurcations.

2023; Sanaga and Howell, 2023; Rosales et al., 2021; Jorba-Cuscó et al., 2018). In the current work, such behavior is also confirmed within the ER3BP, and its relationship to the fold bifurcation is illustrated.

Periodically perturbed systems, including the ER3BP, are generally cast as one-parameter dynamical models. For the ER3BP, with a fixed μ value, the dynamics are governed by a single parameter, e . Seydel (2009) notes that, while fold bifurcations are "generic" (most typical) for one-parameter models, perfect family intersections from perfect pitchfork bifurcations may only exist when some peculiar symmetry is satisfied. Within the CR3BP at a fixed μ value, these perfect bifurcations are more commonly observed (e.g., pitchfork bifurcation from planar Lyapunov orbits to southern and northern halo orbits). On the contrary, these family intersections are expected to exist more sparsely within the ER3BP. A hypothetical perfect crossing within the ER3BP is illustrated in Fig. 19(a), where two families "cross" within the fixed $P = \rho_E$ plane. While these true intersections may exist, they are expected to be sparse and subject to some symmetry properties (Seydel, 2009), e.g., a period-doubling bifurcation within the $P = \rho_E$ plane. Demonstrating the existence of true intersections is beyond the scope of the current work; refer to Seydel (2009) for numerical criteria for discerning true family intersections from fold bifurcations. Within the context of the current investigation, it is sufficient to note that if another nearby family exists that originates from any nearby CR3BP structures, the continuous family is likely to demonstrate broken bifurcations rather than true intersections, as apparent in Fig. 19(b). In a similar context, Jorba-Cuscó et al. (2018) also point out that the lack of symmetry within four-body models may destroy the intersection, resulting in broken bifurcations.

Broken bifurcations are critical in understanding the challenges of numerically transitioning from the CR3BP to HFEM. A smooth continuation process may actually lead to a fundamental change in behavior, deviating from

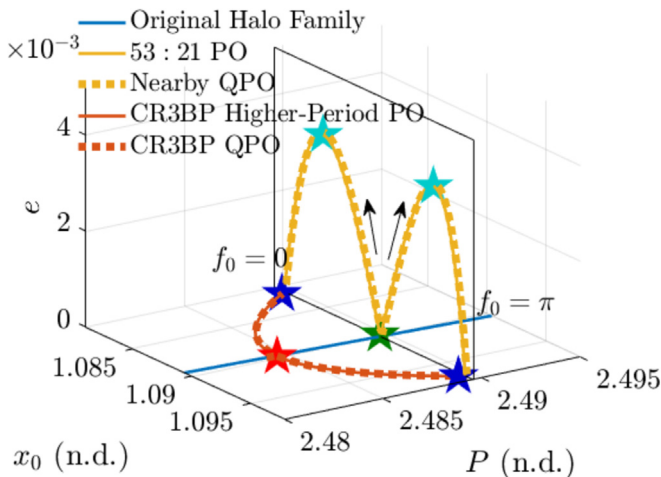


Fig. 20. Fold bifurcation: ER3BP 53 : 21 PO and a nearby QPO bifurcation diagrams.

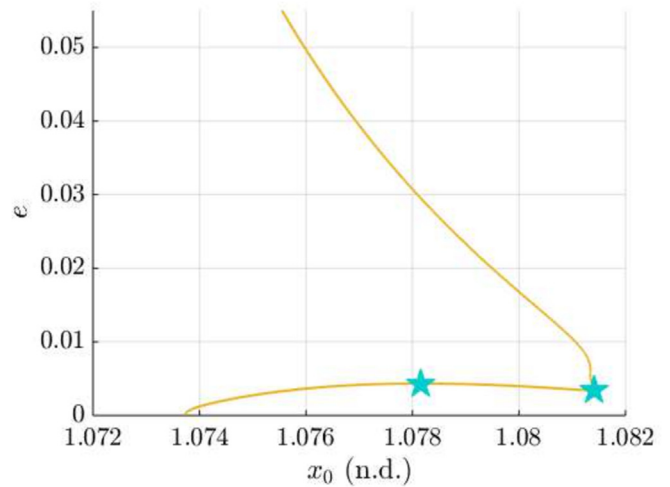


Fig. 21. 14 : 5 PO counterpart 'A', even number of fold bifurcations.

the desired solution geometry as observed in the original CR3BP structure. Also, depending on the shapes of the family hodographs, at certain eccentricity values, the desired "halo-like" structures may cease to exist (Fig. 19(b)). Detecting broken bifurcations, however, is a non-trivial task. Since broken bifurcations involve a smooth family evolution by definition, additional information is necessary to confirm their existence. Potential strategies include exploring different continuation directions (Sanaga and Howell, 2024), introducing additional perturbation parameters (Sanaga and Howell, 2024), and measuring the curvature of the hodograph (Henry et al., 2023). Seydel (2009) acknowledges the general challenges associated with such processes. In the current work, the fold bifurcation is employed as a practical metric to identify potential transition challenges from the CR3BP to the HFEM. Note that the fold bifurcation is not equivalent to broken bifurcations. Broken bifurcations do not necessarily involve a fold in eccentricity, and the presence of a fold bifurcation alone does not confirm a broken branch. However, in cases where the fold bifurcation eventually returns back to zero ($e = 0$), as commonly observed in the Earth-Moon L₂ halo family, the hodograph exhibits at least one broken bifurcation. This broken bifurcation links the original CR3BP halo family to a distinct CR3BP structure associated with the constant ρ branch.

Recall that the HFEM analogs for the Earth-Moon L₂ halos evolve in the vicinity of the ER3BP structures at a realistic eccentricity level, e.g., $e_d = 0.055$. The fold bifurcation, as depicted in Fig. 17(b), illustrates one possible dynamical behavior that impedes the construction of the ER3BP structures at the desired eccentricity value at $e_d = 0.055$ and, hence, the characterization of the HFEM analogs. In the representative bifurcation behavior in Fig. 17(b), the continuous family within the ER3BP in yellow does not reach $e_d = 0.055$ without connecting back to $e = 0$. This trait implies that an eventually successful smooth transition process may require leveraging a nearby

period-multiplied PO or a QPO associated with the center mode of the original CR3BP halo orbit, indicating that the CR3BP PO itself potentially does not serve as a suitable initial guess for the transition process. It is also possible that the structures corresponding to the original CR3BP L₂ halo disappear within the ER3BP that, potentially, also destroy the long-term solution basin within the HFEM, i.e., true HFEM L₂ halo analogs may not exist for some cases within Interface Region. This possible scenario is also illustrated via the continuation examples in Figs. 10 and 12; the evolution from the CR3BP to HFEM with more continuous steps eventually halts, alluding to a potential boundary formed by fold bifurcations within the HFEM dynamics.

6.2.5. Example - ER3BP 53 : 21 PO and a Nearby QPO

Illustrative bifurcation diagrams appear in Fig. 20 that demonstrate a fold bifurcation within the ER3BP. The solid yellow line in the plot represents a resonant ratio PO with $p : q = 53 : 21$ associated with $P \approx 2.48956$ n.d., and the dotted yellow markers indicate a nearby QPO associated with $P \approx 2.48963$ n.d.. Both counterparts for $f_0 = 0$ and $f_0 = \pi$ (from the green star) exhibit a fold bifurcation, \star . It is noted that the local extrema eccentricity values for the two counterparts differ slightly in general. Following the fold bifurcations, the ER3BP structures return to the CR3BP plane, i.e., $e = 0$, bifurcating to the CR3BP branch (\star) through the resonance bifurcation. Tracking this CR3BP branch in red within Fig. 17(b), the structure reconnects with the original CR3BP L₂ halo family through either a period-multiplying or the Hopf bifurcation (\star). Similar to the nominal case depicted in Fig. 17(a), the resonant ratio PO and a nearby QPO exhibit similar behavior in terms of hodographs.

6.3. Additional scenarios

While two illustrative cases are discussed, other cases do exist that exhibit more complex bifurcation behavior and

do not precisely adhere to the two patterns visualized in Fig. 17. Some of these additional cases and their implications for the HFEM transition process are also examined here.

First, the continuation process occasionally reaches $e = 0.055$ but with a non-zero, even number of fold bifurcations. One such example is plotted in Fig. 21, corresponding to the 14 : 5 ratio PO, counterpart 'A'. It is observed that two fold bifurcations appear along the continuation process, marked with \star ; however, the evolution is continuous and reaches the desired $e_d = 0.055$ at the end of the evolutionary process. Consequently, this case does not align with either of the scenarios described in Fig. 17. For this specific case, it is not immediately clear whether a broken bifurcation occurs leading to a nearby CR3BP structure. Note that this scenario rarely occurs within the Earth-Moon L₂ halo orbit family. The two PO counterparts associated with $f_0 = 0$ and $f_0 = \pi$ typically exhibit similar behavior in terms of two representative bifurcation patterns, where the shapes of the hodographs are generally similar and typically involve fold bifurcations at approximately equivalent eccentricity values. However, this similarity is not guaranteed. An example illustrating this variation is provided in Fig. 22 that highlights two counterparts for the 29 : 10 PO. Notably, the two counterparts exhibit very distinct behavior within the hodograph, with differences in the first fold bifurcation eccentricity value and the total number of fold bifurcations. Moreover, the second counterpart displays much more complex bifurcation behavior. While the diagrams in Fig. 17 illustrate representative cases, more complex behaviors occasionally exist even for the same numerical continuation scheme. Similar intricate behavior is expected for the CR3BP constant ρ branch, corresponding to the red curve within Fig. 17(b). This branch may also undergo multiple bifurcations before ultimately reaching the original CR3BP halo family within the hodograph. The potential complexity of the bifurcation behavior underscores the necessity for a simple metric, with the fold bifurcation emerging as a practical tool.

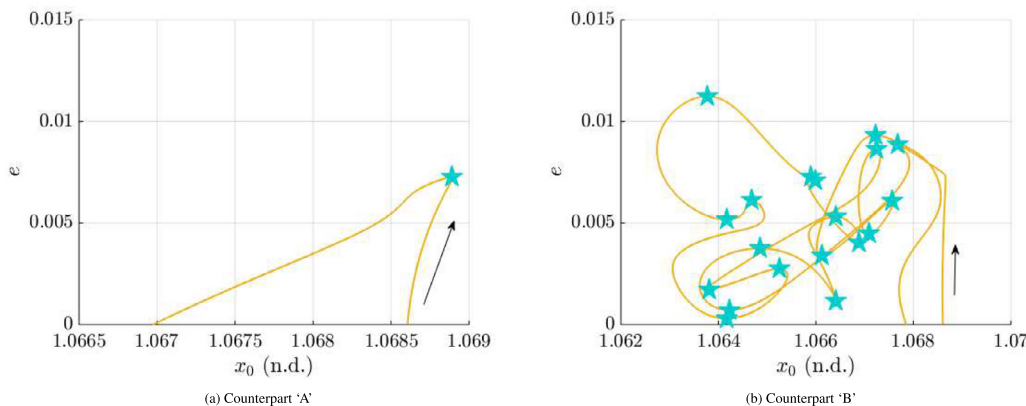


Fig. 22. ER3BP 29 : 10 PO, two counterparts with distinct hodographs.

6.4. Numerical challenges

The detection of the fold bifurcation is contingent on the specific numerical continuation formulations. The present work leverages a perpendicular crossing for the continuation process in the evolution of ER3BP POs, assuming that the family members evolve while reflecting a mirror configuration across the $\hat{x} - \hat{z}$ plane (further detailed in B). Eliminating this assumption potentially reveals more fold bifurcations that connect to non-symmetric structures. Additionally, a denser step size in the continuation process potentially exposes more broken bifurcations. An example is illustrated for the 73 : 24 ratio ER3BP PO in Fig. 23, where three different branches are located with three different step sizes. Leveraging larger step sizes often "jumps" across the broken branches and does not detect them, as demonstrated by Branch 3. On a similar note, a natural parameter continuation procedure, as opposed to pseudo-arclength continuation, is more capable of jumping between disconnected branches, in general. Thus, defining "true" bifurcation diagrams is challenging due to the multiple factors in the numerical procedure. However, a qualitative analysis on the proliferation of broken bifurcations, or alternatively, fold bifurcations, remains possible.

While the ER3BP QPOs exhibit behavior similar to the nearby ER3BP POs, as demonstrated via a sample ratio as illustrated in Fig. 20, QPO construction often encounters challenges prior to reaching the exact fold bifurcation. A numerical limit for QPO computation generally arises when invariant curves become too complex to be accurately represented by a finite number of discretized points. An example is illustrated for $p : q = 59 : 21$ and a nearby QPO in Fig. 24. While both hodographs display similar behavior, the QPO computational limit is reached before the PO fold bifurcation (\star) occurs in the periodic orbit family. Although using different values for invariant curve discretization alleviates the problem locally, QPO

continuation typically fails eventually, as approaching the fold bifurcation typically involves a qualitative behavioral change in the structures where the invariant curves become complex for the employed GMOS QPO computation algorithm. Thus, while both POs and QPOs are leveraged in the current work to provide a more holistic investigation, POs generally offer more accurate bifurcation information, and QPOs complement the information from the PO analysis.

6.5. Global trend for fold bifurcations across the family

The bifurcation behavior for the Earth-Moon L₂ halo family within the ER3BP is globally examined in comparison with the HFEM solution behavior from Fig. 8, focusing on the existence of fold bifurcations. The global trend across the family is depicted in Fig. 25, with the corresponding $p : q$ values within the ranges identified in Table 3. Different combinations of $p : q$ that result in coprime numbers are selected. The CR3BP halo orbits corresponding to these resonant ratios are continued with the numerical scheme outlined in B. The vertical axis of the plot corresponds to the range of e values under consideration, with the maximum value set at $e_d = 0.055$. Note that each PO ratio has two counterparts, and these counterparts may exhibit unique bifurcation behavior, as noted in Fig. 22. Cyan markers (\star) denote the eccentricity value that corresponds to the minimum first fold bifurcation eccentricity for both counterparts. In cases where only one of the counterparts exhibits a turn in eccentricity, that specific eccentricity is marked. If both counterparts undergo fold bifurcations, the smaller eccentricity value from the two turning eccentricity values is marked. Two yellow markers indicate $p : q$ ratios where both counterparts reach e_d at the end of the continuation process. The first type (●) achieves e_d without any fold bifurcation as illustrated in Fig. 18. The second type (\star) involves an even number of fold bifurca-

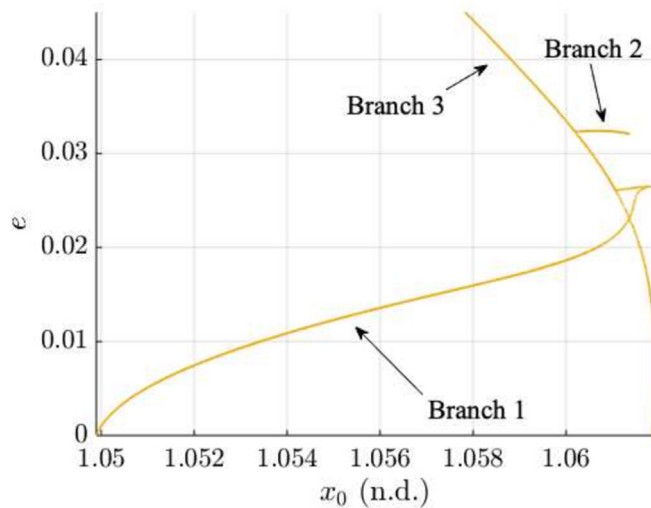


Fig. 23. ER3BP 73 : 24 PO counterpart 'A', different branches located via different step sizes.

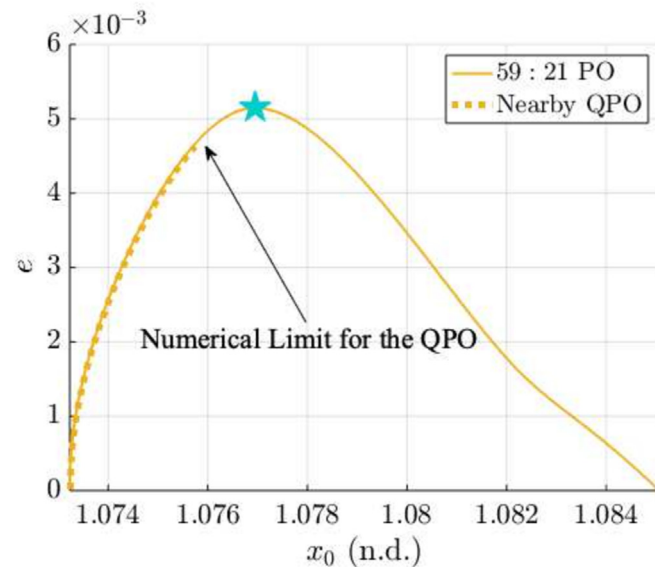


Fig. 24. 59 : 21 PO counterpart 'A' and a nearby QPO.

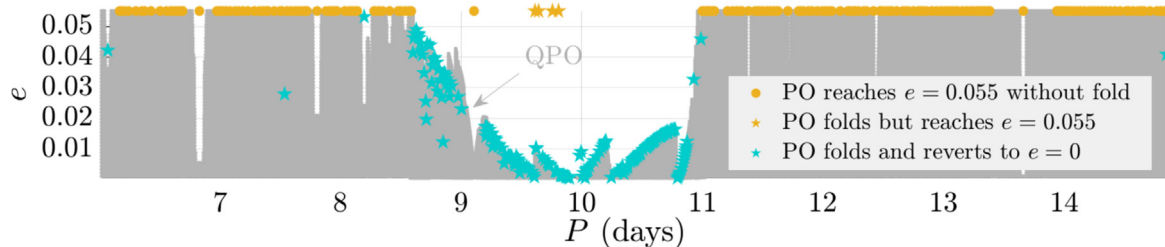


Fig. 25. Global bifurcation trend for POs and QPOs across the Earth-Moon L_2 halo family within the ER3BP.

Table 3
Range for $p : q$ values

Periods (days)	Range for p	Range for q
$P < 8.6$	$p \leq 60$	$q \leq 30$
$8.6 \leq P \leq 11.0$	$p \leq 100$	$q \leq 50$
$11.0 < P$	$p \leq 50$	$q \leq 25$

tions until the continuation process reaches e_d as depicted in the example illustrated in Fig. 21. For some higher values of p , the continuation procedure occasionally diverges due to numerical sensitivities. Such cases are not represented in Fig. 25.

The intermediate region from $P = 8.6$ to 11.0 days are characterized by the existence of fold bifurcations (\star) at $e < 0.055$ and the evolution back to zero eccentricity. Beyond this period range, both shorter and longer periods, the yellow markers (\bullet) govern the behavior, i.e., this continuation scheme reaches e_d without any fold bifurcations. Generally, these markers for the PO continuation align well with adjacent QPO eccentricity boundaries, colored in grey. The QPO boundaries note the maximum eccentricity value before the continuation exhibits a turn in eccentricity or fails to converge due to the complex shape of the invariant curve. In Fig. 25, for the regions where QPOs successfully continue and reach e_d , the yellow markers (\bullet) proliferate, and vice versa. From Fig. 8, these yellow markers (\bullet) correspond to the regions where multi-year HFEM counterparts are readily computed with the CR3BP orbit geometry as the initial guesses. **Therefore, the proliferation of ER3BP PO fold bifurcations before reaching e_d successfully predicts challenges in HFEM transition.** Alternatively, similar behavior is inferred from QPO continuation bound-

aries. For the Earth-Moon L_2 halo family, this transition-challenging region corresponds to orbital periods between 8.6 and 11.0 days.

While the majority of cases adhere to the described pattern, there are exceptions that deviate. Some instances exist outside the challenging domain where a fold bifurcation still occurs when $e < 0.055$. For example, the $p : q = 9 : 2$ sidereal resonant periodic orbit displays this behavior (note that this ratio is different from the synodic 9:2 ratio), where one counterpart at $P \approx 6.07$ days folds at $e \approx 0.04$, despite being outside the problematic region. Upon closer examination of the transition-challenging region in Fig. 26, certain $p : q$ ratios indeed reach $e = 0.055$ without reverting to zero eccentricity. For instance, the ratio near $P \approx 9.1$ days corresponds to the 3 : 1 sidereal resonance, allowing both counterparts to reach e_d without encountering fold bifurcations (\bullet). Additionally, between 9.5 and 10.0 days, four yellow markers (\star) indicate instances where one of the counterparts reaches e_d with an even number of fold bifurcations. It is worth noting that the QPO boundaries exhibit slight deviations from the PO fold bifurcations, particularly for $P < 9.0$ days, where the QPO continuation strategy (grey) achieves higher eccentricity values as compared to the PO continuation. This discrepancy is attributed to the presence of multiple broken branches, and the effective step sizes between the PO and QPO continuation processes are marginally different. Consequently, both continuation processes may trace "continuous" branches from potentially multiple broken branches, as illustrated in Fig. 23. Despite these exceptions and numerical challenges, it remains noteworthy that the *proliferation* of fold bifurcations within the ER3BP is anticipated to signal challenges in the CR3BP to HFEM transition process.

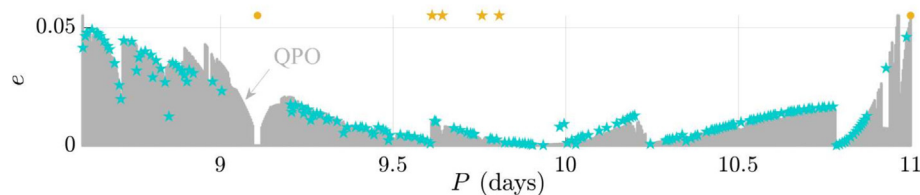


Fig. 26. Global trend across the Earth-Moon L_2 halo family: zoomed-in view in the Interface Region.

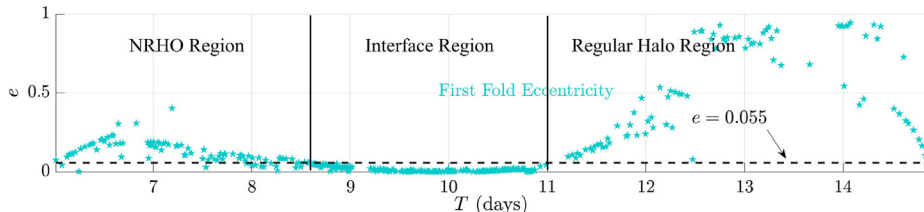


Fig. 27. First fold bifurcation eccentricity values across various ER3BP PO families - examination for higher eccentricity values.

6.6. Fold bifurcations at higher eccentricity values

While the desired eccentricity value, $e_d = 0.055$, represents a realistic Earth-Moon system value, it is possible to further continue from the yellow markers (●) in Fig. 25 until the first fold bifurcation is located for each ratio. The outcomes are depicted in Fig. 27, illustrating that all ratios exhibit turns in eccentricity before $e = 0.99$, or a value near unity. It is expected that these ER3BP structures are eventually linked back to the nearby CR3BP POs as generally depicted in Fig. 17(b). The transition-challenging region in the Earth-Moon L₂ halo family, located between 8.6 and 11.0 days, exists as a specific area where these fold bifurcations occur *before* reaching the desired eccentricity value, $e_d = 0.055$, thus, resulting in some numerical transition challenges from the CR3BP to HFEM. It is also noteworthy that the NRHO region ($P < 8.6$ days) is characterized by smaller values of eccentricity at the fold bifurcations as compared to the region defined by $P > 11.0$. The analysis in the current section indicates that the fold bifurcation is a common behavior for this specific orbit family. This finding potentially indicates that the transition-challenging behavior likely exists for other multi-body systems with higher eccentricity values. Future investigations are warranted to confirm the existence of such behaviors in other systems as well as the specific orbital structures that are more susceptible to the fold bifurcations and the transition-challenging behaviors.

6.7. Potential mitigation strategies

The transition-challenging region is defined by a proliferation of fold bifurcations that impedes the construction of the ER3BP counterparts at a desired eccentricity value, i.e., $e_d = 0.055$. In encountering these fold bifurcations, the following strategies emerge as alternatives to produce ER3BP structures at e_d that potentially serve as updated initial guesses for the HFEM transition process.

6.7.1. Leveraging nearby CR3BP structures

Nearby CR3BP structures are utilized, taking the 5:2 sidereal resonant halo orbit as an example. The hodograph along the $f_0 = 0$ PO counterpart is illustrated in Fig. 28(a) for the 5:2 ratio. Following the fold bifurcation (★), the ER3BP continuation process returns back to $e = 0$, arriving at a nearby CR3BP PO (★). Utilizing this neighboring

structure as a starting point allows for continuation in e , resulting in a hodograph as depicted in Fig. 28(a). Another branch is then continued, eventually reaching e_d at ●. It is noteworthy that at ★, the initial true anomaly, f_0 , is shifted from 0 to π to enable the construction of the new branch, essentially leveraging the alternative counterpart. The orbit geometry at the end of continuation process corresponding to e_d is plotted in Fig. 28(b). It is possible to employ a similar process for the turned structures that frequently occur in Fig. 25; identifying nearby CR3BP POs and their corresponding counterparts within the ER3BP at e_d is possible and may serve as a better initial guess for HFEM analogs. However, these nearby structures are inherently associated with multiple lobes as apparent from Fig. 28(b) that typically spread in the \hat{y} -direction and may destroy the favorable orbit structure offered by the original CR3BP halo orbit.

6.7.2. Jumping to the other broken branch

As an alternative to the proceeding approach, it is possible to deliberately jump to the opposite broken branch, one that *potentially* exists throughout a higher range in e that continues to a value $e_d = 0.055$. This behavior is illustrated in Fig. 29 for the $p : q = 19 : 6$ ratio counterpart 'A'. With the original continuation scheme, only the yellow branch is located. Near the fold bifurcation (★), the sharp turn implies the potential presence of the other branch; a natural parameter continuation scheme with respect to the eccentricity, rather than the pseudo-arclength continuation scheme, is leveraged to locate the other broken branch, as indicated by the arrow denoting the jump direction. The geometry is successfully reproduced at $e = 0.055$ with this strategy, and finally appears as plotted in Fig. 29 (b). Although multiple authors (Henry et al., 2023; Sanaga and Howell, 2024) offer methods to locate the broken branches, the branch may not exist at all. Seydel (2009) further emphasizes the element of chance, stating that "good luck is also needed,"² as the existence and location of the other branch are not known *a priori*. Thus, while the results within Fig. 29 illustrate one successful example, it may not always be successful for other ratios that exhibit fold bifurcations.

² page 210 from Seydel (2009)

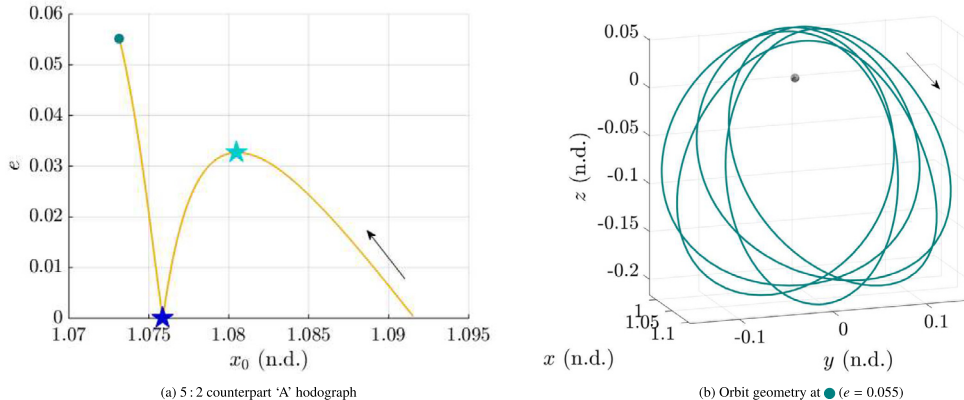


Fig. 28. ER3BP 5 : 2 PO continuation leveraging a nearby CR3BP higher-period PO.

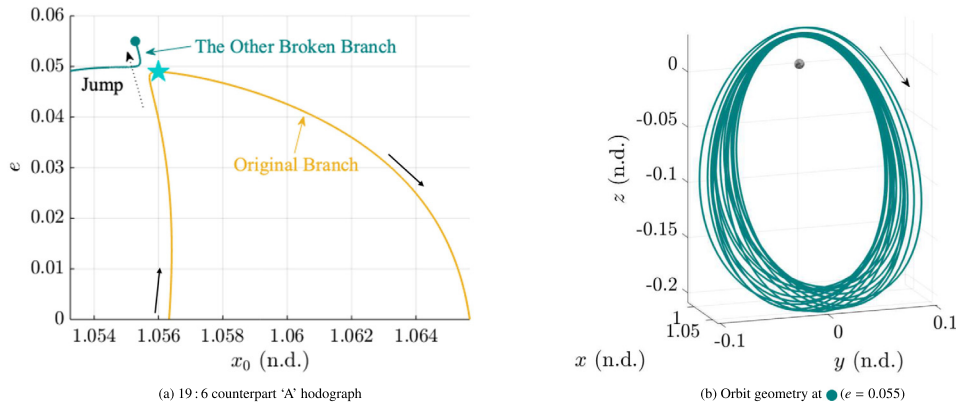


Fig. 29. ER3BP 19 : 6 PO jumping to the other broken branch.

6.7.3. Continuation in μ

While the current investigation assumes that the μ parameter is fixed within the ER3BP, it also serves as possible additional modeling parameter. This extra dimension introduces a distinct continuation direction, allowing different branches to connect at various μ values. As illustrated in Fig. 30, three different μ values are explored to demonstrate varying bounding eccentricity values within the transition-challenging period range, as zoomed in Fig. 26. The selected values are $\mu = 0.1$ (approximately the Pluto-Charon system), $\mu \approx 0.0125$ (the Earth-Moon system value), and $\mu = 0.001$ (approximately the Sun-Jupiter system). Although smaller μ values are more common for Sun-planet and planet-moon systems within the solar system, these three values are selected in proximity to the Earth-Moon system value. The markers in Fig. 30 depict the end of the continuation process: if a fold bifurcation is located for either counterpart before reaching $e_d = 0.055$, such a value is marked. If the continuation reaches e_d , it is also marked. The plots demonstrate that the bounding eccentricity values are slightly altered for different μ values, as expected. However, the proliferation of

fold bifurcations in the vicinity of the original range in period is also common for these nearby μ values. The larger μ value appears to shift the fold bifurcations to higher e values, and conversely, the smaller μ value results in a shift to lower e values. While this example hints at the potential usefulness of an additional search direction in μ , further investigation is required to validate its effectiveness in providing ER3BP structures at e_d for the Earth-Moon system mass ratio, $\mu \approx 0.0125$.

6.7.4. Continuation in P

The fold bifurcations in Fig. 26, or the bounding eccentricities, are determined through a continuation procedure in e , where a continuation in P may assist in connecting to higher eccentricity values. Note that this strategy is potentially useful for the QPO computation, but may not be applicable for the PO computation as the ER3BP POs exist at discrete $p : q$ ratios that do not allow continuation in P . Alternatively, other periodically perturbed models, aside from the ER3BP, facilitate continuation in P , even for the POs. For instance, the Hill Restricted Four-Body Problem (Sanaga and Howell, 2023) scales the independent

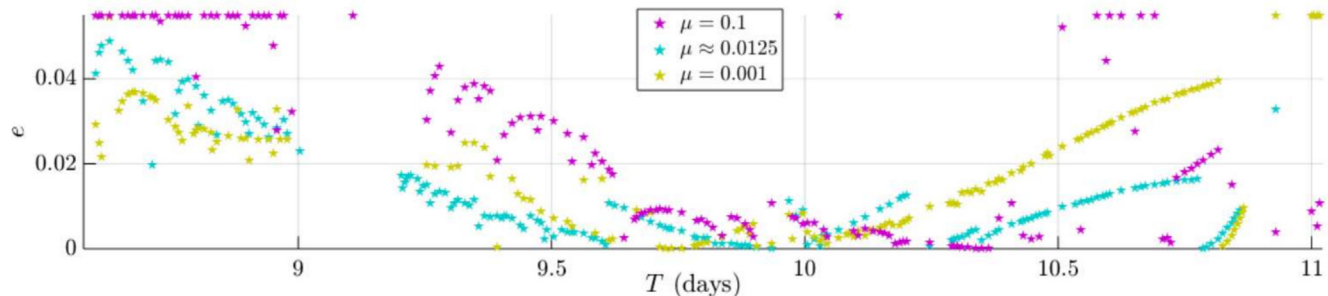


Fig. 30. First fold bifurcation eccentricity values for the ER3BP PO families constructed at three different sample μ values - examination for Interface Region ($8.6 \leq T \leq 11$ days).

variable itself as a function of the sidereal to synodic periods as the model parameter m varies; this parameter controls the pulsation of the Earth-Moon system and shifts P as well (Sanaga and Howell, 2023; Sanaga and Howell, 2024). A continuation in P within the ER3BP may or may not be linked to the continuation of the model parameter m within the HR4BP and further analysis is warranted.

7. Concluding remarks

The current work focuses on the numerical investigation of analogs for Earth-Moon Circular Restricted Three-Body Problem (CR3BP) L_2 halo orbit family within a Higher-Fidelity Ephemeris Model (HFEM). Multi-year counterparts are produced via a numerical process leveraging the CR3BP halo orbits as initial guesses, where distinct regions are identified along the halo family, highlighting an Interface Region where challenges arise in constructing long-term solutions and the converged solutions significantly deviate from the original CR3BP geometry.

For deeper insights into the behavior of the HFEM analogs, the Elliptic Restricted Three-Body Problem (ER3BP) is employed. For the entire family, the similarities between the solutions from the HFEM and Quasi-Periodic Orbits (QPOs) within the ER3BP are investigated through hyperplane examination and Fourier analysis. It is observed that the HFEM analogs are most significantly influenced by the realistic pulsation of the Earth-Moon system, with the ER3BP providing valuable approximations for this perturbed environment.

The ER3BP bifurcation behavior along the continuation process is a crucial metric for addressing the transition-challenging dynamics from the CR3BP to HFEM. In the Earth-Moon system, with eccentricity as the continuation parameter, the proliferation of fold bifurcations before reaching a desired eccentricity at $e = 0.055$ is identified as a key behavior, illustrated within the L_2 halo orbit family. In the period range $8.6 \leq P \leq 11.0$ days, fold bifurcations frequently manifest at $e < 0.055$, creating continuous connections between ER3BP structures and nearby CR3BP structures. This region aligns with the previously identified transition-challenging Interface Region. Therefore, fold bifurcations within the ER3BP prove to be an effective metric for anticipating transition challenges within the ER3BP

alone, eliminating the need for extensive numerical transition experiments from the CR3BP to the HFEM.

Declaration of Competing Interest

The authors declare that they have no known competing financial interests or personal relationships that could have appeared to influence the work reported in this paper.

Acknowledgments

The first author would like to thank Kwanjeong Educational Foundation for the financial support. Portions of this work are also supported by Purdue University and under Grant NASA JSC 80NSSC18M0122. Valuable discussions are appreciated with past and former members from Multi-Body Dynamics Research Group, including Rohith Reddy Sanaga, Dhruv Jain, Juan-Pablo Almanza-Soto, Dale Williams, and Dr. Brian McCarthy.

Appendix A. Eigenstructure of the Monodromy Matrix at a Fold Bifurcation within the ER3BP

When the hodographs from a family of ER3BP POs demonstrates a local extrema, the eigenstructure of the monodromy matrix, M , includes a unity eigenvalue pair at that exact location. First, an augmented fixed point for the ER3BP PO is denoted as $\vec{s}_+(\gamma)$, where γ corresponds to an arbitrary monotonically evolving parameter that governs the family evolution, e.g., an arclength defined along a hodograph from the initial bifurcating point along the family of periodic orbits in the CR3BP (\star in Fig. 17). Note that the vector is seven-dimensional, i.e., $\vec{s}_+ \in \mathbb{R}^7$, including the state vector and the scalar eccentricity value associated with each fixed point. Thus,

$$\vec{s}_+(\gamma) = \begin{bmatrix} \vec{s}(\gamma) \\ e(\gamma) \end{bmatrix}, \quad (\text{A.1})$$

where $\vec{s}(\gamma)$ and $e(\gamma)$ correspond to the six-dimensional fixed point state and the eccentricity in the intermediate model, respectively. Then, assume that at $\gamma = \gamma^*$, a turn in eccentricity occurs. (The asterisk denotes the turn location.) The nearby fixed point is then represented as,

$$\vec{s}_+(\gamma^* + \delta\gamma) = \vec{s}_+^* + \delta\vec{s}_+ \approx \vec{s}_+^* + \begin{bmatrix} \delta\vec{s} \\ 0 \end{bmatrix}, \quad (\text{A.2})$$

where δ denotes a small increment. Subsequently, consider an augmented periodic mapping function $\vec{\psi}_+(\vec{s}_+) = \vec{s}_+$ with a fixed period corresponding to $P = 2\pi q$ for a resonant ratio $p : q$. The seven by seven monodromy matrix \mathbf{M} is defined as $\mathbf{M} = \frac{d\vec{\psi}_+}{d\vec{s}_+}(\vec{s}_+)$. While $\vec{\psi}_+$ is a time-dependent function, the initial true anomaly is fixed as f_0 and does not explicitly appear as an additional parameter. The structure of the augmented monodromy matrix \mathbf{M}_+ is,

$$\mathbf{M}_+ = \begin{bmatrix} \mathbf{M} & \frac{\partial\vec{\psi}}{\partial e}(\vec{s}) \\ 0_{1 \times 6} & 1 \end{bmatrix}, \quad (\text{A.3})$$

where the upper left matrix is the six by six monodromy matrix and the bottom right is always unity, as the eccentricity does not depend on the state, \vec{s} . Then, for the nearby fixed point, the mapping function results in,

$$\vec{\psi}_+(\vec{s}_+^* + \delta\vec{s}_+) = \vec{s}_+^* + \delta\vec{s}_+. \quad (\text{A.4})$$

The linear approximation leads to,

$$\begin{aligned} \vec{\psi}_+(\vec{s}_+^* + \delta\vec{s}_+) &\approx \vec{\psi}_+(\vec{s}_+^*) + \frac{d\vec{\psi}_+}{d\vec{s}_+}(\vec{s}_+^*)\delta\vec{s}_+ \\ &= \vec{s}_+^* + \mathbf{M}_+^*\delta\vec{s}_+ = \vec{s}_+^* + \delta\vec{s}_+. \end{aligned} \quad (\text{A.5})$$

Thus, the following expression is produced,

$$(\mathbf{M}_+^* - \mathbf{I}_+)\delta\vec{s}_+ = 0, \quad (\text{A.6})$$

where \mathbf{I}_+ is a seven-by-seven identity matrix. From the structure of \mathbf{M}_+ and the assumption of the turn in eccentricity,

$$(\mathbf{M}_+^* - \mathbf{I}_+)\delta\vec{s}_+ = \begin{bmatrix} \mathbf{M}^* - \mathbf{I} & \frac{\partial\vec{\psi}}{\partial e}(\vec{s}^*) \\ 0_{1 \times 6} & 0 \end{bmatrix} \begin{bmatrix} \delta\vec{s} \\ 0 \end{bmatrix} = \vec{0}, \quad (\text{A.7})$$

where \mathbf{I} is a six-by-six identity matrix. This equation reduces to,

$$(\mathbf{M}^* - \mathbf{I})\delta\vec{s} = \vec{0}. \quad (\text{A.8})$$

Thus, at the fold bifurcation, $\lambda = 1$ and $\delta\vec{s}$ always appear as eigenvalue and eigenvector for the six-by-six monodromy matrix, \mathbf{M} . As the ER3BP is a symplectic dynamical model, there exists a pair of unit eigenvalues at the fold bifurcation.

Appendix B. Numerical continuation scheme

B.1. ER3BP PO continuation

For the ER3BP PO associated with the $p : q$ resonant ratio, the total period is $2q\pi$. Leveraging the perpendicular crossing at the half period, the total propagation time is $q\pi$. Then, a multiple shooting scheme is employed where n segments are equally split out with respect to the independent variable between f_0 and $f_0 + q\pi$ within the ER3BP. The free variable vector for the targeter is constructed as,

$$\vec{X} = [x_0, z_0, (dy/df)_0, \vec{s}_2^\top, \dots, \vec{s}_n^\top, e]^\top, \quad (\text{B.1})$$

where $x_0, z_0, (dy/df)_0$ correspond to the non-zero fixed point components at f_0 . The subsequent states corresponding to segments from 2 to n are denoted as \vec{s} with appropriate subscripts. The last component in the vector \vec{X} is the scalar eccentricity value associated with each PO. The constraint vector appears,

$$\vec{F} = [\vec{F}_c^\top, \vec{F}_p^\top]^\top, \quad (\text{B.2})$$

where the subscripts c and p correspond to the continuity between the segments and the perpendicular crossing at the end of the propagation sequence from the last segment at $f_0 + q\pi$, respectively. An ER3BP PO results in a zero constraint vector, i.e., $\vec{F} = \vec{0}$. For the $p : q$ ratio, the number of segments is assigned as $n = 2p + 1$. Note that the lengths of \vec{X} and \vec{F} are $6n - 2$ and $6n - 3$, respectively; thus, the Jacobian of \vec{F} with respect to \vec{X} generally allows a one-dimensional null space. This null space vector is denoted as \vec{V}_N with a length of $6n - 2$. Then, a pseudo-arclength continuation scheme enforces the following additional scalar constraint.

$$F_N = \Delta\vec{X}^\top \vec{V}_N - ds = 0, \quad (\text{B.3})$$

where $\Delta\vec{X}$ is the change in the free variable vector from the previously converged solution and ds is a user-defined nondimensional step size within the targeting process. The continuation process solves for \vec{X} that satisfies Eqs. (B.2) and (B.3). Following discussions from Section 6.4, relevant factors for the continuation results include the number of segments (n) and the step size (ds). Larger n and smaller ds values result in a higher likelihood of locating additional fold bifurcations within the ER3BP PO continuation process as it results in denser effective step sizes with respect to e . While there exists no “correct” combination of values, the following set of parameters are utilized for the continuation scheme here: $ds = 0.001$ and $n = 2p + 1$.

B.2. ER3BP QPO continuation

The GMOS algorithm employs a stroboscopic map with a fixed time interval P . At each stroboscopic time, the longitudinal angle (θ_P) remains constant and the remaining latitudinal angle, θ_E , governs the invariant curve on the map. This curve is denoted as $\vec{u}(\theta_E)$ and represents the 6-dimensional state for the spacecraft position and velocity at the map crossing. To approximate the invariant curve, N discrete points correspond to evenly spaced angles $\theta_E \in [0, 2\pi]$ as $\theta_{E,k} = 2\pi k/N$ for $0 \leq k \leq N - 1$. In the current work, $N = 51$ is leveraged. From N guesses for the state along the invariant curve constructed at $\theta_{E,k}$, Fourier coefficients \vec{C}_k are constructed via the Discrete Fourier Transform (DFT). Then, with these coefficients, the invariant curve is approximated as a truncated Fourier series,

$$\vec{u}(\theta_E) \approx \sum_{k=0}^{N-1} \vec{C}_k \exp(i\theta_E k). \quad (\text{B.4})$$

Here, “exp” corresponds to the exponential function and $i = \sqrt{-1}$. Then, at the map, the state remains indefinitely on the invariant curve, where θ_E shifts by ρ_E for each return. This invariance condition is, then, posed as,

$$\Psi_{\theta_E}(\vec{u}(\theta_E)) = \vec{u}(\theta_E + \rho_E), \quad (\text{B.5})$$

where Ψ_{θ_E} refers to the stroboscopic flowmap that integrates $\vec{u}(\theta_E)$ from $f = \theta_E$ to $f = \theta_E + P$. In addition to this constraint, a phase constraint is enforced on θ_P to prevent the algorithm from detecting the same QPO associated with a different θ_P value. Such a formulation follows one developed by Olikara and Scheeres (2012). Thus, an iterative Newton–Raphson process is leveraged to search for N 6-dimensional states that satisfy the invariance and phase constraints. Thus, the free variable vector is constructed as,

$$\vec{X} = [\vec{s}_{Q,1}^T, \vec{s}_{Q,2}^T, \dots, \vec{s}_{Q,N}^T, e], \quad (\text{B.6})$$

where \vec{s}_Q denotes the discrete points along the approximated invariant curve. Similar to the PO continuation, e corresponds to the model eccentricity. The constraint vector is then,

$$\vec{F} = \left[\vec{F}_{\text{invariance}}^\top, \vec{F}_{\text{phase}}^\top \right]^\top, \quad (\text{B.7})$$

where “invariance” and “phase” correspond to the invariance condition and the phase constraint as discussed above. Note that the lengths of \vec{X} and \vec{F} are $6N + 1$ and $6N + 1$, respectively. This formulation still allows a one-dimensional null space, as there exists a general ambiguity in the phase information for the longitudinal angle, θ_P , discussed in detail by Olikara and Scheeres (2012). Thus, one more constraint is typically required to make the targeting problem fully constrained. In the current work, two formulations are leveraged. The first approach enforces the scalar constraint $F_e = e - e_{\text{fix}} = 0$, corresponding to a natural parameter continuation along the model eccentricity. The second method enforces the pseudo-arclength continuation as described by Eq. (B.3). These two methods are employed together in the current work to produce the ER3BP QPO continuation results in Fig. 13. Throughout the L₂ halo orbit family, the initial guess construction is initiated from a fixed point at apolune ($\theta_P = 0$) in the CR3BP PO. Originating with a small eccentricity value $e = 1.1 \cdot 10^{-5}$, the initial invariant curve is determined to satisfy the invariance and phase constraints. Then, for the NRHO and Regular Halo Regions, 50 linearly spaced steps in eccentricity are employed for the natural parameter continuation scheme until the eccentricity reaches e_d . Within the Interface Region, however, the natural parameter continuation method terminates early at small values of eccentricity. The pseudo-arclength continuation scheme is leveraged here with $ds = 0.001$, resulting in denser steps in e , as evident in Fig. 13.

References

- Almanza-Soto, J.-P., 2023. Zero-momentum point analysis and ephemeris transition for interior Earth to libration point orbit transfers. M.S. thesis Purdue University Indiana, USA.
- Andreu, M., 1998. The quasi-bicircular problem. Ph.D. dissertation Univ. Barcelona.
- Andreu, M.A., 2003. Preliminary study on the translunar halo orbits of the real earth–moon system. *Celest. Mech. Dynam. Astron.* 86, 107–130.
- Bosanac, N., Cox, A.D., Howell, K.C., et al., 2018. Trajectory design for a cislunar cubesat leveraging dynamical systems techniques: the lunar icecube mission. *Acta Astronaut.* 144, 283–296.
- Boudad, K., Howell, K.C., Davis, D.C., 2022. Analogs for earth-moon halo orbits and their evolving characteristics in higher-fidelity force models. In: AIAA SCITECH 2022 Forum, p. 1276.
- Boudad, K.K., Howell, K.C., Davis, D.C., 2020. Dynamics of synodic resonant near rectilinear halo orbits in the bicircular four-body problem. *Adv. Space Res.* 66 (9), 2194–2214.
- Campagnola, S., Lo, M., Newton, P., 2008. Subregions of motion and elliptic halo orbits in the elliptic restricted three-body problem. In: AAS/AIAA Space Flight Mechanics Meeting.
- Clampin, M., 2008. The james webb space telescope (jwst). *Adv. Space Res.* 41 (12), 1983–1991.
- Crusan, J.C., Smith, R.M., Craig, D.A., et al., 2018. Deep space gateway concept: extending human presence into cislunar space. In: 2018 IEEE Aerospace Conference. IEEE, pp. 1–10.
- Davis, D.C., Phillips, S.M., Howell, K.C., et al., 2017. Stationkeeping and transfer trajectory design for spacecraft in cislunar space. In: AAS/AIAA Astrodynamics Specialist Conference, pp. 1–20.
- Dei Tos, D.A., Toppo, F., 2017. Trajectory refinement of three-body orbits in the real solar system model. *Adv. Space Res.*, 59(8), 2117–2132. URL:<https://www.sciencedirect.com/science/article/pii/S0273117717300868>. doi:10.1016/j.asr.2017.01.039.
- Ferrari, F., Lavagna, M., 2018. Periodic motion around libration points in the elliptic restricted three-body problem. *Nonlinear Dyn.* 93 (2), 453–462.
- Gómez, G., Masdemont, J., Mondelo, J., 2002. Solar system models with a selected set of frequencies. *Astron. Astrophys.* 390 (2), 733–749.
- Gómez, G., Mondelo, J.M., 2001. The dynamics around the collinear equilibrium points of the rtbp. *Physica D* 157 (4), 283–321.
- Gómez, G., Mondelo, J.-M., Simó, C., 2010. A collocation method for the numerical fourier analysis of quasi-periodic functions. i. numerical tests and examples. *Discrete Contin. Dyn. Syst. Ser. B* 14 (1), 41–74.
- Henry, D., Rosales, J., Brown, G., et al., 2023. Quasi-periodic orbits near earth-moon II in the hill restricted four-body problem. International Symposium on Space Technology and Science, Kurume, Japan.
- Jorba, A., Villanueva, J., 1997. On the persistence of lower dimensional invariant tori under quasi-periodic perturbations. *J. Nonlinear Sci.* 7 (5), 427–473.
- Jorba-Cuscó, M., Farrés, A., Jorba, À., 2018. Two periodic models for the earth-moon system. *Front. Appl. Math. Stat.* 4 (32), 1–14.
- Lantoine, G., Russell, R.P., 2011. Near ballistic halo-to-halo transfers between planetary moons. *J. Astronaut. Sci.* 58 (3), 335–363.
- Lian, Y., Gómez, G., Masdemont, J.J., et al., 2013. A note on the dynamics around the lagrange collinear points of the earth-moon system in a complete solar system model. *Celest. Mech. Dynam. Astron.* 115, 185–211.
- Liang, Y., Nicolás, B., Jorba, À., 2021. Leveraging l3 to transfer to l4 in the sun-perturbed earth-moon system. *Acta Astronaut.* 189, 337–348.
- Lujan, D., Scheeres, D.J., 2022. Earth–moon l2 quasi-halo orbit family: characteristics and manifold applications. *J. Guid., Control, Dynam.* 45 (11), 2029–2045.
- Lyons, R.G., 1997. Understanding digital signal processing. Pearson Education India, p. 3/E..

- McCarthy, B.P., 2022. Cislunar trajectory design methodologies incorporating quasi-periodic structures with applications. Ph.D. dissertation Purdue University West Lafayette, Indiana.
- McComas, D., Christian, E.R., Schwadron, N.A., et al., 2018. Interstellar mapping and acceleration probe (imap): a new nasa mission. *Space Sci. Rev.* 214, 1–54.
- Muralidharan, V., Howell, K.C., 2023. Stretching directions in cislunar space: applications for departures and transfer design. *Astrodynamic* 7 (2), 153–178.
- Oguri, K., Oshima, K., Campagnola, S., et al., 2020. Equuleus trajectory design. *J. Astronaut. Sci.* 67 (3), 950–976.
- Olikara, Z.P., 2016. Computation of quasi-periodic tori and heteroclinic connections in astrodynamics using collocation techniques. Ph.D. dissertation University of Colorado at Boulder.
- Olikara, Z.P., Gómez, G., Masdemont, J.J., 2016. A note on dynamics about the coherent sun-earth-moon collinear libration points. In: *Astrodynamics Network AstroNet-II: The Final Conference*. Springer, pp. 183–192.
- Olikara, Z.P., Scheeres, D.J., 2012. Numerical method for computing quasi-periodic orbits and their stability in the restricted three-body problem. *Adv. Astronaut. Sci.* 145 (911–930), 911–930.
- Park, B., Howell, K.C., 2024. Assessment of dynamical models for transitioning from the circular restricted three-body problem to an ephemeris model with applications. *Celest. Mech. Dynam. Astron.* 136 (1), 6.
- Park, B., Sanaga, R.R., Howell, K.C., 2024. A Frequency-Based Hierarchy of Dynamical Models in Cislunar Space: Leveraging Periodically and Quasi-Periodically Perturbed Models. In: PRE-PRINT (Version 1) available at Research Square. <https://doi.org/10.21203/rs.3.rs-4822764/v1>.
- Park, R.S., Folkner, W.M., Williams, J.G., et al., 2021. The jpl planetary and lunar ephemerides de440 and de441. *Astronom. J.* 161 (3), 105. <https://doi.org/10.3847/1538-3881/abd414>.
- Peng, H., Xu, S., 2015. Stability of two groups of multi-revolution elliptic halo orbits in the elliptic restricted three-body problem. *Celest. Mech. Dynam. Astron.* 123 (3), 279–303.
- Peterson, L.T., Rosales, J.J., Scheeres, D.J., 2023. The vicinity of earth–moon l1 and l2 in the hill restricted 4-body problem. *Physica D* 455, 133889.
- Rosales, J.J., Jorba, A., Jorba-Cuscó, M., 2021. Families of halo-like invariant tori around l2 in the earth-moon bicircular problem. *Celest. Mech. Dynam. Astron.* 133 (4), 16.
- Sanaga, R.R., Howell, K.C., 2023. Synodic resonant halo orbits in the hill restricted four-body problem. In: *AAS/AIAA Astrodynamics Specialist Conference*. American Astronautical Society, Austin, Texas.
- Sanaga, R.R., Howell, K.C., 2024. Analyzing the challenging region in the earth-moon l2 halo family through hill restricted four-body problem dynamics. In: *AIAA SCITECH 2024 Forum*.
- Scheuerle Jr, S.T., Howell, K.C., Davis, D.C., 2024. Energy-informed pathways: A fundamental approach to designing ballistic lunar transfers. *Adv. Space Res.*.
- Seydel, R., 2009. Practical bifurcation and stability analysis, volume 5. Springer Science & Business Media.
- Villegas-Pinto, D., Baresi, N., Locoche, S., et al., 2023. Resonant quasi-periodic near-rectilinear halo orbits in the elliptic-circular earth-moon-sun problem. *Adv. Space Res.* 71 (1), 336–354.
- Wang, Y., Zhang, R., Zhang, C., et al., 2021. Transfers between nrhos and dros in the earth-moon system. *Acta Astronaut.* 186, 60–73.
- Wiesel, W.E., Pohlen, D.J., 1994. Canonical floquet theory. *Celest. Mech. Dynam. Astron.* 58, 81–96.
- Williams, D., Howell, K.C., Davis, D.C., 2023. A comparison of station-keeping strategies for halo orbits. In: *AAS/AIAA Astrodynamics Specialist Conference*. Big Sky, Montana.
- Zimovan-Spreen, E.M., Howell, K.C., Davis, D.C., 2020. Near rectilinear halo orbits and nearby higher-period dynamical structures: orbital stability and resonance properties. *Celest. Mech. Dynam. Astron.* 132 (5), 1–25.
- Zimovan-Spreen, E.M., Scheuerle, S.T., McCarthy, B.P., et al., 2023. Baseline orbit generation for near rectilinear halo orbits. *AAS/AIAA Astrodynamics Specialist Conference AAS*, 23–268.